How endosomal PIKfyve inhibition prevents viral membrane fusion and entry

Nicholas Chow[1,$], Gustavo Scanavachi[1,2,3,$], Anand Saminathan[1,2,$] and Tom Kirchhausen[1,2,3,*]

[1]Program in Cellular and Molecular Medicine, Boston Children's Hospital, 200 Longwood Ave, Boston, MA 02115, USA

[2]Department of Cell Biology, Harvard Medical School, 200 Longwood Ave, Boston, MA 02115, USA

[3]Department of Pediatrics, Harvard Medical School, 200 Longwood Ave, Boston, MA 02115, USA

[$] Equal contribution

[*] Corresponding author:
Tom Kirchhausen. Ph.D.
Harvard Medical School
200 Longwood Ave
Boston, MA 02115
kirchhausen@crystal.harvard.edu
phone: +1 617 713 8888 / fax: +1 617 713 8898

Running title: *Swollen Endosomes Block Productive Viral Fusion and Entry*

Key words: *Viral Entry, PIKfyve Inhibition, Endosomal Fusion, Membrane Tension, Lattice Light-Sheet Microscopy*

ABSTRACT

Enveloped viruses enter cells by membrane fusion. The viral membrane fuses with a host membrane, either at the cell surface or within endocytic compartments. For endocytic entry, fusion is typically triggered by low pH and often requires proteolytic priming by compartment-specific host proteases, which together define the site and mechanism of fusion and shape viral tropism.

Inhibition of the lipid kinase PIKfyve, which generates PI(5)P and PI(3,5)P_2 in late endosomes and lysosomes, swells those compartments and blocks infection by a subset of enveloped viruses, including Ebola virus, Marburg virus, coronaviruses (SARS-CoV-2), and VSV chimeras bearing Ebola, SARS-CoV-2, or Lassa glycoproteins, while showing minor effects on H1N1 influenza and no effect on VSV or VSV–rabies chimeras. In the work reported here, we have determined the basis for selectivity.

We show that swelling of late endosomes/lysosomes, independent of changes in lipid composition or altered virion trafficking, is sufficient to block virus–endosome fusion and genome release, even when endosomal acidity is preserved. Acute PIKfyve inhibition with apilimod or brief hypotonic treatment produced endosomal swelling and impaired infection by interrupting a late endosomal entry step. Live-cell 3D lattice light-sheet fluorescence microscopy imaging tracked fluorescent virions accumulating and arresting in late endosomes prior to fusion, and single-cell, single-round assays confirmed loss of infectivity.

These data support a simple biophysical mechanism: endo-lysosomal swelling, likely increasing endosomal membrane tension, creates an energy barrier to fusion and genome release. Inducing such swelling may offer a general strategy to inhibit viruses that depend on late endosomal entry.

SIGNIFICANCE STATEMENT

Why does inhibiting the endosomal lipid kinase PIKfyve, which generates PI(5)P and PI(3,5)P_2, block entry of some enveloped viruses but spare VSV-G? Using single-round infectivity and live-cell 3D imaging, we show that acute PIKfyve inhibition traps incoming VSV chimeras bearing SARS-CoV-2 spike or Ebola GP in swollen late endosomes/lysosomes before fusion and genome release. Hypotonic swelling phenocopies the block, and removing glutamine prevents apilimod-induced swelling and largely restores infection, arguing that swelling—not altered phosphoinositides—restricts entry. We propose a physical mechanism: increased endosomal membrane tension raises the energetic barrier for fusion-pore formation and genome release. Modulating endolysosomal volume may therefore inhibit viruses that rely on late endosomal entry.

INTRODUCTION

Enveloped viruses initiate infection by fusing their membrane with a host-cell membrane, delivering their genetic material into the cytosol (see review (1)). This fusion can occur at the plasma membrane or within endocytic compartments. For many viruses, including filoviruses and coronaviruses that rely on endocytosis, fusion is typically triggered by low endosomal pH and often requires proteolytic priming of viral glycoproteins by endosomal resident host proteases; for some, an additional host factor in the endolysosomal compartment is required (see reviews (2–5)). These spatial and pH dependencies define the site and mechanism of fusion during the early steps of infection, and, ultimately, determine viral tropism and infectivity.

PIKfyve, a lipid kinase on late endosomal and lysosomal membranes, generates phosphatidylinositol 3,5-bisphosphate [PI(3,5)P_2] and phosphatidylinositol 5-phosphate [PI(5)P_2] (6). Its depletion or pharmacological inhibition produces enlarged late endosomes and lysosomes and decreases PI(5)P and PI(3,5)P_2 while increasing PI3P levels by preventing its conversion into PI(3,5)P_2 (7–10); the organelle specificity of these alterations has been confirmed by the localization of optical phosphoinositide biosensors by fluorescence microscopy (11). PIKfyve inhibition blocks infection by a subset of enveloped viruses at early stages of entry. For example, treatment with the PIKfyve inhibitor apilimod prevents GP-mediated entry of filoviruses and SARS-CoV-2 and for VSV- or lentivirus-based pseudotypes, without affecting virion uptake or bulk endosomal acidification (12, 13). Vacuolin-1, which also targets PIKfyve, similarly suppresses single-cycle infection by VSV chimeras bearing Ebola or SARS-CoV-2 glycoproteins by preventing fusion and genome delivery from endolysosomal compartments (13). Other PIKfyve-

directed inhibitors, including YM201636, SGC-PIKFYVE-1I and PIKfyve/PIP5K1C, inhibit early infection by parental African swine fever virus, enteroviruses, and β-coronaviruses, as well as by SARS-CoV-2 spike–pseudotyped virions (14–17). Together, these observations support the view that PIKfyve-activity at late endosomes and lysosomes is a common requirement for successful viral entry. In contrast, PIKfyve inhibition has only modest effects on H1N1 influenza virus infection (18) and little or no effect on viruses whose entry occurs in early endosomes, such as VSV and VSV particles bearing rabies virus G (VSV–RABV) (13).

A recent study identified LYVAC (PDZD8) as the ER-anchored lipid transfer protein that mediates ER-to-lysosome lipid transfer at ER–endolysosome contact sites, enabling osmotic membrane expansion (19). In the absence of LYVAC, apilimod fails to induce lysosomal swelling, supporting a model in which vacuolation primarily and the consequent increase in membrane tension depends on lipid transfer, rather than on loss of PI3P or PI(3,5)P_2. We therefore tested the hypothesis that the antiviral effect of PIKfyve inhibition by apilimod arises primarily from a mechanical constraint on virion fusion to the limiting membranes of the endolysosomal system, rather than from a block in endosomal trafficking or a change in endosomal phosphoinositide composition. We combined quantitative infectivity assays with high-precision, live-cell three-dimensional fluorescence microscopy to track single virions, allowing direct comparison of the effects of apilimod on VSV, VSV–ZEBOV, and VSV–SARS-CoV-2 infection.

Because these viruses share an identical VSV backbone, differences in apilimod sensitivity must arise from how their entry steps respond to perturbation of PIKfyve activity rather than from downstream replication events. Entry of VSV is mediated by its G protein and requires no further proteolysis for activation. Following clathrin-mediated endocytosis, acidification in early and early-late endosomes triggers a conformational change in G that drives membrane fusion (20). In contrast, VSV–ZEBOV requires two sequential processing steps of its GP: cleavage during biosynthesis, followed by cathepsin-mediated trimming in late endosomes or lysosomes to expose the NPC1-binding site. VSV–SARS-CoV-2 likewise depends on sequential proteolysis of its spike protein, furin cleavage at S1/S2 during maturation, followed by TMPRSS2- or cathepsin-mediated cleavage at S2′ and on endosomal acidification (see review (21)).

We show here that endosomal swelling, induced either by apilimod or by hypoosmotic challenge, correlates with inhibition of viral fusion, but only for VSV–ZEBOV or VSV–SARS-CoV-2 virions that reach and attempt fusion within swollen compartments. VSV, which enters from early

129 endosomes that do not swell, escapes this inhibition, as does a subpopulation of VSV–SARS-
130 CoV-2 virions that fuse in early endosomes. We suggest that under these swelling conditions,
131 endolysosomes accumulate solute and water and increase their volume without a fully
132 compensatory increase in membrane area. The resulting rise in membrane tension will oppose
133 the local membrane remodeling required for fusion (1). Increased membrane tension in swollen
134 compartments thus imposes a physical barrier to fusion and thereby accounts for the selective
135 sensitivity of certain viruses to PIKfyve inhibition.

136 **RESULTS**

137 **Apilimod inhibits infection by VSV-eGFP-SARS-CoV-2 and VSV-MeGFP-ZEBOV but not by**
138 **VSV-eGFP-G**

139 We first confirmed that infection by VSV-SARS-CoV-2 or VSV-ZEBOV requires PIKfyve activity,
140 whereas infection by VSV-G does not. We inoculated Vero cells not expressing TMPRSS2 with
141 three recombinant VSVs: (i) VSV-eGFP-G, which expresses soluble eGFP and the parental VSV
142 G protein; (ii) VSV-eGFP–SARS-CoV-2, which expresses soluble eGFP and in which the SARS-
143 CoV-2 spike replaces G; and (iii) VSV-MeGFP–ZEBOV, which expresses eGFP fused to the viral
144 matrix protein (M) and carries the Zaire ebolavirus GP instead of G. All three viruses deliver their
145 genomes into the cytosol via endosomal fusion: for VSV, fusion is directly triggered by low pH,
146 whereas Ebola and SARS-CoV-2 Spike first require their proteolytic activation by endosomal
147 proteases, whose activity also requires low pH (13).
148
149 We measured infectivity in Vero cells using a single-cell imaging assay that reports expression of
150 virally encoded cytosolic eGFP or MeGFP (13), following the incubation protocol shown in Fig.
151 1A. To assess the role of endosomal PIKfyve on infection, we treated the Vero cells with apilimod,
152 a selective inhibitor of PIKfyve lipid kinase activity (22). As shown in Figs. 1B-D, apilimod fully
153 inhibited infection by VSV-eGFP–SARS-CoV-2 and VSV-MeGFP–ZEBOV but had no effect on
154 VSV-eGFP-G.
155

156 **Compartment-specific endosomal swelli**ng

157 Apilimod treatment of SVG-A cells co-expressing gene-edited fluorescent chimeras of mScarlet-
158 EEA1 (a marker of early endosomes) and NPC1-Halo (a marker of late endosomes and
159 lysosomes) causes swelling of the latter compartment(s), but not of the former (13). We confirmed
160 here that we can detect this compartment-specific swelling in SVG-A cells by lattice light-sheet
161 microscopy (LLSM) (Fig. S1). After apilimod treatment, endosomes labeled with mScarlet alone
162 remained as small, diffraction limited puncta, while those labeled with NPC1-Halo, as well as
163 those containing both labels, became substantially enlarged.
164
165 We examined dose dependence of enlargement as follows. We loaded cells with Alexa Fluor
166 568-labeled dextran (Dextran-AF568), which accumulates in late endosomes and lysosomes, and
167 measured the radii of individual endolysosomes across a range of apilimod concentrations (Fig.
168 2). In untreated cells, late endosomes and lysosomes had a narrow distribution of radii centered
169 at ~0.5μm (range 0.3-1.0μm: Fig. 2 B, C). Apilimod induced a concentration-dependent increase

170 in radius, yielding a bimodal distribution with peaks centered at ~0.75μm and at ~1.25μm.
171 Applying a 90th percentile cutoff (0.725μm) to score a position as "swollen" yielded the dose-
172 dependent frequency of enlargement shown in Fig. 2 C, D.
173
174 **Apilimod-induced late-endosomal swelling inhibits entry of VSV-MeGFP-ZEBOV and VSV-**
175 **eGFP-SARS-CoV-2 but not of VSV itself**
176 We verified that incoming VSV-MeGFP-ZEBOV particles reach NPC-1 compartments under our
177 experimental conditions by using LLSM with genome-edited SVG-A cells expressing NPC1-Halo
178 (13) labelled with Janelia Fluor 646 HaloTag ligand. Cells were exposed to virions for 10 min,
179 washed, and imaged 40 min or 4 hrs. later at 37 °C, according to the protocol in Fig. 3A. At a
180 multiplicity of infection (MOI) of ~0.5, each cell imaged at 40 min post inoculation contained 25–
181 30 fluorescent virions in NPC1-positive compartments (Fig. 3B, D). Productive genome entry,
182 monitored by the appearance of MeGFP fluorescence at the nuclear margin (13), was apparent
183 4 h post-inoculation (Fig. 3E) but not 50 min post-inoculation (Fig. 3B). These observations are
184 consistent with the expectation that ZEBOV GP fuses from late endosomes (23, 24).
185
186 In the presence of 5 μM apilimod, virions trafficked efficiently to NPC1-positive compartments
187 within 50 minutes (Fig. 3C, D), despite pronounced late endosome and lysosome enlargement,
188 showing that PIKfyve inhibition had not disrupted traffic from the cell surface. At 4 h post-
189 inoculation, however, the apilimod-treated cells showed no MeGFP signal at the nuclear periphery
190 (Fig. 3F) and failed to support infection (Fig. 3G). That is, PIKfyve inhibition blocked viral genome
191 release from a (swollen) late endosomal compartment, in agreement with our published
192 observations (13). Infection efficiency decreased with increasing apilimod concentration and
193 endosomal swelling (Fig. 2E, G), further supporting the conclusion that late endosomal
194 enlargement impairs fusion and genome release.
195
196 VSV–SARS-CoV-2 entry can proceed through either a full low-pH and cathepsin-dependent
197 stage, in cells lacking TMPRSS2, or a pathway requiring activation by TMPRSS2 on the cell
198 surface (25–27). SARS-CoV-2 entry is apilimod sensitive in cells that lack TMPRSS2 (Fig. 1C),
199 but only partially so in cells that express the protease (28) (Fig. 4, 0% hypo). Thus, when
200 TMPRSS2 is present, the virus appears to follow both entry pathways, and fusion can occur either
201 at the plasma membrane or in early endosomes, after TMPRSS2 cleavage, or alternatively in
202 acidic late endosomes, following cathepsin activation. In its absence, entry is restricted to the late
203 endosomal/lysosomal, cathepsin-dependent route.

204

205 We confirmed that apilimod does not inhibit infection by VSV–eGFP–G (Fig.1B) and correlated
206 its resistance with entry from early endosomes. We monitored fusion and cytosolic release, using
207 VSV–PeGFP–G. Expression of eGFP fused to the viral phosphoprotein (P) allowed us to
208 discriminate between fluorescent virions within NPC1-tagged endosomes and those whose
209 genome was released into the cytosol. SVG-A NPC1-Halo–expressing cells were pulse-
210 inoculated and imaged by LLSM at 30- and 40-minutes post-inoculation, with or without 5 μM
211 apilimod (Fig. 5A–C). After 30 min and in both conditions, 8–96 virions per cell had trafficked to
212 NPC1-positive compartments, and ~20% of P-spots associated with the viral genome had been
213 released into the cytosol (Fig. 5D–F). These results indicate that genome release occurs in early
214 endosomes, with a subset of virions becoming trapped in late endosomes. The similar fraction of
215 cytosolic particles in apilimod-treated and untreated cells is consistent with the resistance of VSV-
216 G–mediated infection to PIKfyve inhibition and agrees with similar results obtained in prior
217 infectivity studies (13).
218

219 **Endosomal swelling by ammonium accumulation, not PI(3,5)P_2 loss, accounts for**
220 **blockage of VSV–MeGFP-ZEBOV infection by PIKfyve inhibitors**

221 Under normal conditions, cytosolic glutamine is converted in mitochondria to glutamate and NH_3,
222 which enters endosomes and lysosomes, where acidification by the endo-lysosomal V-ATPase
223 traps it as NH_4^+ (29). PIKfyve inhibition induces endo-lysosomal swelling through ammonium
224 accumulation and water influx, an effect prevented by glutamine withdrawal from the medium
225 (29) or by inhibition of the V-ATPase (30). We took advantage of this relationship to distinguish
226 between a biochemical consequence of PI(3,5)P_2 depletion by acute apilimod treatment from a
227 broader physical block to infection caused by endosomal swelling, by testing whether the
228 blockade of infection could be reversed by limiting ammonium accumulation.
229

230 To validate our experimental system, we imaged SVG-A cells in FluoroBrite medium containing
231 apilimod, with or without supplementation with 4 mM glutamine and FBS. Late endosomes and
232 lysosomes were labeled with internalized Dextran-568 (Fig. 6A). As expected, apilimod-induced
233 endosomal swelling, visually monitored for up to 30 min, was markedly reduced in glutamine-free
234 medium (Fig. 6B). Based on this observation, we inoculated cells for 30 min with VSV-MeGFP-
235 ZEBOV in standard buffer (e.g. containing glutamine), followed by a 30 min incubation with
236 apilimod in the presence or absence of glutamine. Glutamine and 50 nM apilimod were then
237 added for the remainder of the assay to restrict the test of viral entry to the 30 min post-inoculation

window, comparing the effect with and without glutamine (Fig. 6C). This step was necessary because prolonged incubation in glutamine-free medium during early infection blocked synthesis of MeGFP encoded by VSV-MeGFP–ZEBOV. VSV-MeGFP–ZEBOV infection was reduced by ~60% in the presence of both glutamine and apilimod but was minimally affected in glutamine-free medium with apilimod (Fig. 6C–E). These results suggest that inhibition of infection arises from endosomal swelling itself, rather than from loss of PI(3,5)P_2-dependent signaling.

Hypotonic-induced endolysosomal swelling reduces VSV-MeGFP–ZEBOV and VSV-eGFP–SARS-CoV-2 infection

To test directly whether endolysosomal osmotic swelling impairs viral entry, we used a non-pharmacological method to enlarge endosomes and lysosomes during the early phase of infection. Brief incubation of cells in hypotonic medium induces transient swelling of the cytoplasm and intracellular membrane-bound compartments, most prominently late endosomes and lysosomes (31–33). We exploited this osmotic effect to perturb the entry process of VSV-eGFP-G, VSV-MeGFP–ZEBOV and VSV-eGFP–SARS-CoV-2. A single 30-minute hypotonic pulse, initiated 30 minutes post-inoculation, was reversible, did not lead to cell death (Fig. 4B) consistent with prior reports showing no overt toxicity from a similar transient osmotic shock (34), and targeted the entry window while minimizing artifacts from subsequent volume regulation. VSV-eGFP-G infection remained unchanged with or without the treatment (Fig. 4C).

To quantify endosomal swelling, we incubated Vero cells in medium diluted with increasing amounts of water and measured endolysosomal size by spinning-disk confocal imaging of cells preloaded with Alexa Fluor 568–labeled dextran (Dextran-AF568; Fig. 7A). Using the same 90th percentile radius cutoff (0.725 μm) as in the apilimod experiments, we observed a modest increase in enlarged compartments with 30% dilution and a robust increase with 60% dilution, whereas 10% dilution had no detectable effect (Fig. 7B–D).

We next tested the impact of this hypotonic swelling on infection. SVG-A or Vero cells were inoculated with VSV-MeGFP–ZEBOV, VSV-eGFP–SARS-CoV-2, or VSV-eGFP-G, then subjected to 30-minute hypotonic treatments at the indicated dilutions (Figs. 7E-G and 8). To restrict continued viral fusion after the swelling phase, we added Bafilomycin A1 alone (VSV-G), apilimod alone (VSV-MeGFP-ZEBOV) or in combination with apilimod (VSV-SARS-CoV-2) immediately following the hypotonic pulse. Bafilomycin A1 blocks endosomal acidification (35) and thereby prevents low pH-dependent viral membrane fusion. The combination of

272 Bafilomycin A1 and apilimod inhibited fusion of VSV-MeGFP–ZEBOV and VSV-eGFP–SARS-
273 CoV-2. Infection of SVG-A cells by VSV-MeGFP–ZEBOV dropped to ~40% of control levels
274 following 60% dilution, with no inhibition at lower dilutions (Fig. 7F and G). The same treatment in
275 Vero cells suppressed infection by ~ 50% for both VSV-eGFP–SARS-CoV-2 and VSV-MeGFP–
276 ZEBOV but had no effect on VSV-eGFP (Fig. 8B-D). The similarity between these results and
277 those obtained with apilimod supports the conclusion that late endosomal swelling mediated by
278 transient hypotonicity rather than inhibition of a specific biochemical pathway selectively blocks
279 infection by viruses that require trafficking to late endosomes, preventing membrane fusion and
280 cytosolic genome delivery.
281
282 To test whether hypotonic treatment inhibits infection primarily through late endosomal swelling,
283 we took advantage of the differential activation of SARS-CoV-2 spike (S): TMPRSS2 activates S
284 at the cell surface/early endosomes, whereas cathepsins do so in late endosomes (25–27). In
285 Vero cells ectopically expressing TMPRSS2, concurrent treatment with camostat (a TMPRSS2
286 inhibitor that prevents early entry) and apilimod (which blocks late entry) completely inhibited
287 VSV-SARS-CoV-2 infection (Fig. 4A–C) (28). Either compound alone caused the expected partial
288 inhibition (~60% for apilimod, ~25% for camostat) consistent with additive effects on distinct entry
289 routes (Fig. 4C) (28).
290
291 If hypotonic swelling acts primarily in late endosomes, infection should be strongly inhibited when
292 TMPRSS2 is absent or blocked by camostat, and only weakly inhibited when TMPRSS2 is active.
293 Our results matched these predictions: 60% hypotonic treatment inhibited infection by 50-60%
294 either without TMPRSS2 (Fig. 7D) or with TMPRSS2 plus camostat (Fig. 4C), but only by ~20%
295 when TMPRSS2 was present without camostat (Fig. 4C). Consistent with late-endosomal fusion,
296 combining hypotonic treatment with apilimod did not further reduce infection (~60%, Fig. 4C).
297 Conversely, by preventing early entry, camostat sensitized infection to hypotonic swelling (~20%
298 without vs ~ 60% with camostat, Fig. 4C). Together, these results support our inference that
299 hypotonic swelling blocks infection by interfering with the late endosomal entry pathway.
300
301 **Free and membrane-bound VSV-MeGFP–ZEBOV virions in swollen endosomes**
302 Finally, we assessed whether VSV-MeGFP–ZEBOV virions remain membrane-bound under
303 swelling conditions that block infection using live-cell 3D LLSM imaging of virions within apilimod-
304 induced, enlarged NPC1-Halo containing late endosomes and lysosomes in SVG-A cells (Figs.
305 3C, F and 9). We did not use hypotonic swelling because both transience and heterogeneity limit

306 resolution and stability during live-cell imaging. In non-swollen endosomes (~300-500 nm
307 diameter), the point-spread function of the microscope precludes distinguishing virions at the
308 limiting membrane from those in the lumen (Figs. 3B, E). In contrast, apilimod-induced swelling
309 yields larger endosomes of ~1 μm diameter (Figs. 3C, F), enabling spatial separation of
310 membrane-bound and luminal particles (Figs. 3C, F and 9). Because these compartments remain
311 acidic (12), we expected most virions to remain receptor-bound and fusion-competent.
312
313 We used 3D live-cell LLSM to quantify the movement of fluorescent virions inside swollen
314 endolysosomal compartments labeled with endogenously tagged NPC1-Halo in SVG-A cells (Fig.
315 9). Treatment with 5 μM apilimod produced largely immobile enlarged endosomes, in contrast to
316 the dynamic trafficking observed in untreated cells. Visual inspection of z-projected 3D time series
317 revealed that ~75% of 859 fluorescent VSV-MeGFP–ZEBOV virions localized to the lumen while
318 the 25% remainder colocalized with the limiting membrane (Fig. 9B, C, F). A similar distribution
319 of virions in the lumen was also observed for VSV-PeGFP-G, which is not sensitive to apilimod
320 treatment (Fig. 9F). In that case, ~25% of 590 virions remained membrane bound while the rest
321 were in the lumen. These observations were unexpected.
322
323 To distinguish luminal from membrane-associated behavior, we tracked the 3D positions of
324 individual VSV-MeGFP–ZEBOV particles over time. Using time-resolved LLSM at 4-second
325 intervals, we followed fluorescent virions within swollen compartments and computed their mean
326 squared displacement (MSD) (representative examples depicted in the insets in Fig. 9). Particles
327 localized to the lumen had nearly constant MSD values (Fig. 9B), consistent with the confinement
328 within a spherical volume, as expected from a plateau value of $6/5\,R^2$ (Fig. 9D). In contrast,
329 particles stably associated with the limiting membrane showed constrained motion and MSD
330 profiles consistent with movement of the surface of a rotating sphere (Fig. 9C, E). Variation in
331 particle and compartment dynamics resulted in diverse trajectory patterns. We restricted this
332 analysis to representative examples, as current computational limitations precluded automated
333 processing of larger datasets.
334
335 We interpret these single-virion imaging results as follows. In normal acidic endosomes, VSV-
336 eGFP-P-G and VSV-MeGFP–ZEBOV remain stably associated with their respective receptors.
337 VSV-G–mediated fusion occurs primarily in early endosomes, which are not subject to osmotic
338 swelling. Because NPC1 is absent from this compartment, VSV-MeGFP–ZEBOV fusion does not
339 occur there. As VSV-eGFP-P-G and VSV-MeGFP–ZEBOV virions traffic further, arrival in swollen

340 late endosomes correlates with a loss of stable membrane association. We attribute this shift to
341 increased membrane tension, which could impede viral fusion by raising the energetic barrier to
342 the membrane deformations required for hemifusion and full fusion (see Discussion).
343
344 In the acidic environment of swollen endosomes, unbound viral glycoproteins in VSV-PeGFP-G
345 or VSV-MeGFP–ZEBOV that have not yet engaged the limiting membrane may undergo a
346 premature low pH–induced conformational change, thus making them unable to rebind and no
347 longer capable of driving fusion. Our data do not imply that swelling intrinsically impairs fusion-
348 peptide exposure or insertion for virions that remain membrane engaged; the “bound” population
349 stays attached to the limiting membrane and can, in principle, insert the fusion peptide upon low-
350 pH activation. Rather, swelling allows us to detect a “loose” luminal virus population whose GP
351 presumably can undergo low-pH triggering without membrane contact, leaving GP in a post-
352 trigger, nonproductive state because the fusion peptide cannot insert into the target membrane in
353 trans. This mechanism would therefore explain both the retention of virions at the membrane and
354 the release of others into the lumen, where they become fusion-incompetent and unable to rebind.
355 For VSV-G, this has little consequence, as fusion typically occurs in the early endosome, e.g.
356 upstream of this compartment. In contrast, for VSV-MeGFP-ZEBOV, the combination of altered
357 membrane mechanics and disrupted NPC1 engagement in late endosomes likely underlies the
358 observed failure to fuse and the consequent block in infection.

359 **DISCUSSION**

360 We examined why inhibition of the endosomal lipid kinase PIKfyve selectively blocks infection by
361 certain membrane-enveloped viruses, represented here by VSV chimeras bearing the SARS-
362 CoV-2 spike or Ebola virus GP, while leaving parental VSV-G–mediated infection unaffected.
363 Using a combination of quantitative infectivity assays and high-precision, live-cell 3D imaging, we
364 identified a previously unrecognized and mechanistically simple explanation: endosomal
365 membrane swelling acts as a biophysical barrier to viral fusion and genome delivery into the
366 cytosol.
367
368 Previous models have attributed the antiviral effects of PIKfyve inhibition primarily to disruptions
369 in endosomal maturation or impaired trafficking of virions to protease-rich, fusion-competent
370 compartments. While consistent with the dependence of SARS-CoV-2 and Ebola virus on late
371 endosomal cathepsin activity and NPC1 function, these models do not account for our earlier
372 observations by live-cell single virion fluorescence microscopy, confirmed here, that these virions
373 trafficked normally to the swollen NPC1-positive compartments under PIKfyve inhibition but failed
374 to initiate productive infection.
375
376 Our findings uncouple PI(3,5)P_2 depletion from the block in viral infection. Although apilimod
377 inhibits PIKfyve and reduces PI(3,5)P_2 levels, the antiviral effect against VSV-SARS-CoV-2 and
378 VSV-ZEBOV requires endosomal swelling, a process driven by glutamine-dependent
379 accumulation of NH_4^+ and consequent osmotic influx. Apilimod treatment in glutamine-depleted
380 media failed to block infection, indicating that PI(3,5)P_2 loss alone is insufficient to impair viral
381 entry. Furthermore, endosomal pH reporters show that apilimod treatment causes at most a
382 modest decrease in endolysosomal luminal pH, arguing that inhibited entry is not due to loss of
383 acidity (36–38). These observations implicate a mechanical disruption of the fusion-permissive
384 environment, rather than defects in endosomal acidification. Thus, the antiviral activity of apilimod
385 depends on a biophysical alteration of endosomal membranes rather than solely on
386 phosphoinositide depletion.
387
388 We further demonstrated that transient hypotonic late endosome swelling, in the absence of
389 PIKfyve inhibition, phenocopies the antiviral effect, reinforcing our conclusion that osmotic
390 expansion of endosomal volume rather than disruption of lipid signaling impairs viral entry. These
391 observations together with our observation that apilimod did not hinder the traffic of VSV-G, VSV-
392 ZEBOV or VSV-SARS-CoV2 to the endolysosomal compartment (this study and see also (13))

strengthen the conclusion that the key barrier is not trafficking or maturation failure, but instead a tension-induced mechanical resistance of the endosomal membrane to the deformation required for fusion and pore formation. Fusion requires precise spatial coordination between viral and host membranes, and a membrane environment permissive for local deformation. Swollen endosomes may resist the bending and curvature of the limiting membrane necessary for pore formation, particularly for glycoproteins with stringent conformational checkpoints, such as VSV-G, EBOV-GP, or SARS-CoV-2 spike.

Pore formation during virus–endosome fusion imposes a substantial elastic cost because the membrane must pass through highly curved, nanometer-scale intermediates. In our system, we take the bending/elastic work required to reach a pore-competent state as $G_{pore} \approx 43–65\ k_B T$. A minimal energetic comparison asks whether the fusion machinery can supply at least this amount. For influenza, used here as the best studied virus example, multiple analyses indicate that productive fusion requires the concerted action of roughly three HA trimers (39–41). A commonly used estimate for the free-energy drop per HA trimer upon completion of the fusogenic refolding (extended intermediate → postfusion hairpin) is ~34 ± 3 $k_B T$ (42) , giving $G_{HA}(3) \approx 3 \times 34 \approx 102\ k_B T$ (roughly 92–112 $k_B T$). On this accounting, three trimers can, in principle, cover the pore-bending requirement and leave a residual margin $G_{margin} = G_{HA}(3) - G_{pore} \approx 37 – 59\ k_B T$ to pay other contributions along the pathway. Membrane tension (γ) directly consumes this margin because it adds an area work term to any intermediate that effectively increases membrane area by ΔA, $\Delta G\gamma \approx \gamma\Delta A$.

Two observations argue that the resting limiting membrane of endosomes/lysosomes already operates near the boundary of available slack area. First, because we cannot measure γ directly on small organelles, we use Fluorescence Lifetime Imaging Microscopy (FLIM) values from Lyso Flipper/Flipper-TR targeted to endosomal organelles as an operational reporter of membrane mechanical state (43, 44). Flipper-TR at the cell surface was calibrated in cells by correlating its FLIM values with cell surface membrane tension inferred from tether forces during osmotic perturbations, establishing a monotonic lifetime–tension relationship that approached a high-tension regime as membranes exhaust slack area (44). Lyso Flipper lifetimes of control endolysosomes fall in this high-lifetime regime (43, 45–47), consistent with a “taut” limiting membrane even before swelling. Second, ultrastructure from electron microscopy (9) showed smooth limiting membranes with limited folded/tubular reserve in the endosomes of control cells, again arguing against significant stores of excess area in control conditions and smooth

427 membranes with no folded/tubular membranes during pharmacological inhibition of PIKfyve
428 (vacuolin-1)-mediated distension, also consistent with “taut” membranes.
429
430 Thus, acute osmotic swelling should raise membrane tension (γ) because luminal volume
431 increases faster than the limiting membrane can acquire new area. Under constrained area
432 supply, swelling imposes areal strain, $\varepsilon = \Delta A/A_0$, and increases tension approximately as $\Delta\gamma \simeq$
433 $K_A\varepsilon$, with $K_A \approx 250 \pm 50$ mN·m⁻¹. Even $\varepsilon = 0.02$ yields $\Delta\gamma \approx 5$ mN·m⁻¹, placing the limiting
434 membrane in a near-maximal-stretch regime. At these tensions, the area work competes directly
435 with the energy margin available from three HA trimers. Requiring $G_{margin} \gtrsim \gamma\Delta A$ gives $\gamma_{max} \approx (37–$
436 $59)\ k_B T / \Delta A$. For a conservative nanometer-scale $\Delta A \sim 50–100$ nm², $\gamma_{max} \approx 1.5–4.9$ mN·m⁻¹.
437 Thus, if swelling elevates γ to ~5 mN·m⁻¹, the tension term alone costs $\Delta G_\gamma \approx 60\ k_B T$ for $\Delta A = 50$
438 nm² (and ≈120 $k_B T$ for $\Delta A = 100$ nm²), exhausting or exceeding the residual budget after paying
439 G_{pore}. Under these swollen conditions, three HA trimers cannot supply enough additional work to
440 drive pore formation unless more HA participate, ΔA is substantially smaller, or local tension is
441 transiently relieved.
442
443 Although similar constraints on fusion energetics and copy number have been quantified for
444 SNARE-driven fusion (with estimates that roughly 2-3 SNARE complexes are required for content
445 mixing (48)), comparable quantitative bounds are not yet available for the fusion glycoproteins of
446 VSV, SARS-CoV-2, or Ebola virus. We nevertheless infer that the same physical constraint
447 applies for these virions. This tension–energy budget therefore provides a parsimonious
448 mechanistic explanation for why acute endosomal swelling suppresses entry virion entry
449 pathways that normally proceed in relatively non-swollen compartments and thereby prevents
450 infection.
451
452 Why is infection by VSV-G unaffected by apilimod treatment or osmotic swelling? The simplest
453 explanation is that VSV-G–mediated fusion and genome release occur in early endosomes, which
454 are not subject to PIKfyve-dependent swelling. Indeed, previous studies using dominant-negative
455 Rab GTPase mutants showed that VSV infection is inhibited by Rab5(S34N), but not by
456 Rab7(T22N), indicating that fusion occurs before endosomal maturation into Rab7-positive
457 compartments (49–51). Inhibition of PIKfyve kinase by apilimod, at the concentrations used here,
458 also had a minimal effect on influenza-virus infection (18), consistent with the effect of dominant-
459 negative Rab5 and Rab7 GTPase mutants indicating that fusion can occur in both early and late
460 endosomes (51); because apilimod does not swell early endosomes, this route remains available

461 for productive fusion. Our proposed mechanism for apilimod resistance is further supported by
462 our finding that apilimod-mediated inhibition of VSV-SARS-CoV-2 infection is only partial in cells
463 expressing TMPRSS2 and only becomes complete in its absence (this study, see also (28)).
464 TMPRSS2-mediated activation of the SARS-CoV-2 spike promotes fusion at the plasma
465 membrane or within early endosomes, bypassing the late endosomal route (25–27). Accordingly,
466 in TMPRSS2-negative cells where both VSV-SARS-CoV-2 and VSV-ZEBOV rely on late
467 endosomal fusion, the extent of inhibition by osmotic challenge is similar. Thus, viral fusion is
468 governed not solely by pH or receptor engagement but also by the trafficking itinerary of the virion
469 and the mechanical state of the endosomal membrane at the site of fusion.
470
471 Many enveloped viruses, including filoviruses, coronaviruses, and arenaviruses rely on late
472 endosomal or lysosomal compartments for entry (see review (52)), making them potentially
473 sensitive to perturbations in membrane mechanics. Targeting host pathways that regulate
474 endosomal membrane tension, such as PIKfyve or its lipid effectors, offers a mechanistically
475 distinct antiviral strategy, one that does not interfere with receptor binding or protease activation,
476 but instead acts at the level of fusion competence. By identifying membrane tension as a key
477 regulator of viral entry, our study highlights the utility of integrating biophysical parameters into
478 models of intracellular viral trafficking and fusion.

MATERIAL AND METHODS

Detailed material and methods are presented in Appendix SI. Briefly, we carried out single-round infection, endolysosome swelling, and virus-tracking experiments using Vero-derived and SVG-A cell lines, including gene-edited SVG-A cells expressing EEA1–mScarlet and NPC1–HaloTag. We used VSV chimeras bearing native VSV-G or substituted glycoproteins (SARS-CoV-2 S or Ebola virus GP) and propagated them in Vero E6 monolayers. For infection assays, we adsorbed virus for 30 min, removed unbound particles by washing, incubated for ~7–8 h, fixed with paraformaldehyde, and scored infection by eGFP positivity relative to nuclear counts.

To perturb endolysosomal physiology, we inhibited PIKfyve with apilimod in the presence or absence of glutamine or instead imposed transient hypotonic shock; where indicated, we used bafilomycin A1 or camostat. We labeled endolysosomes with internalized fluorescent dextran or NPC1–Halo ligand and quantified compartment size and virus colocalization by 3D fluorescence microscopy (spinning-disk confocal) and lattice light-sheet imaging. We tracked individual virions in 3D, quantified motility by mean square displacement, and used simulations to interpret confinement and endosome-rotation–driven behavior. Image segmentation and quantification used FIJI/LabKit and custom MATLAB workflows; statistics used one-way ANOVA.

Statistical Analysis

Statistical comparisons between control and experimental groups were performed using one-way ANOVA (parametric). Significance levels are indicated by asterisks: *$p < 0.05$; **$p < 0.01$; ***$p < 0.001$; ****$p < 0.0001$. Comparisons without annotated p-values were not statistically significant.

Materials, Data, and Code Availability

Requests for VSV chimeras and their material transfer agreements should be directed to and will be fulfilled by Dr. Sean Whelan, spjwhelan@wustl.edu. Datasets and custom analysis code are available at https://github.com/kirchhausenlab. For further information, please contact the lead author at kirchhausen@crystal.harvard.edu.

ACKNOWLEDGMENTS

We thank S.C. Harrison for editorial help, S. Whelan for support, M. Cornejo Pontelli for generously providing stocks of VSV chimeras used in this study, E. Sitarksa for imaging the samples used for the endolysosome enlargement assay, B. Zuniga for assistance with determination of virus concentration, and members of the Kirchhausen laboratory for support and encouragement. We also acknowledge the L. Lavis lab and the Open the Chemistry team (Janelia Research Campus, HHMI) for the generous gift of Hoechst Janelia 646 and Janelia Fluor 646 (JF646) dyes. The research was supported by a National Institute of General Medical Sciences Maximizing Investigators' Research Award GM130386 to T. Kirchhausen and AI163019-05 NIH/NIAID Grant Award to S. Whelan and T. Kirchhausen.

The Zeiss Lattice Lightsheet 7 microscope, located in the IID-HSPH BSL-3 Imaging Core established in 2024 at the Harvard Chan School, was acquired with generous funding from the Massachusetts Life Sciences Center to S. Fortune and T. Kirchhausen. Acquisition of the computing hardware including the DGX's GPU-based computers, CPU clusters, fast access memory, archival servers, and workstations that made possible this study was supported by generous grants from the Massachusetts Life Sciences Center to T. Kirchhausen and by an equipment supplement to the National Institute of General Medical Sciences Maximizing Investigators' Research Award GM130386 to T. Kirchhausen. Construction of the server room housing the computing hardware was made possible with generous support from the PCMM Program at Boston Children's Hospital.

The authors declare no competing financial interests.

Author contributions: N. Chow, G. Scanavachi, A. Saminathan and T. Kirchhausen conceptualized and designed the experiments; N. Chow and A. Saminathan carried the cell biological experiments; G. Scanavachi carried the optical image analysis. T. Kirchhausen drafted the manuscript and revised it in close consultation with all co-authors.

535 **FIGURES**

536 **Figure 1. Apilimod inhibits infection by VSV chimeras bearing SARS-CoV-2 or ZEBOV**
537 **glycoproteins, but not by VSV-G.**

538 **(A)** Schematic of the infection assay. Vero cells lacking TMPRSS2 were pretreated with 5 μM
539 Apilimod for 1 h, followed by a 30-min incubation with VSV-eGFP-G, VSV-eGFP–SARS-CoV-2,
540 or VSV-MeGFP–ZEBOV at an approximate MOI of 0.5. in the continued presence of 5 μM
541 apilimod. Unbound virus was removed by three consecutive washes (each containing 5 μM
542 apilimod), and cells were maintained in 5 μM apilimod throughout the experiment. At 7.5 h
543 postinfection, cells were fixed, and infection was quantified as the percentage of eGFP-positive
544 cells relative to total nuclei (Hoechst Janelia 646 stain), using automated image analysis encoded
545 by a script in FIJI.

546 **(B–D)** Representative maximum intensity z-projections (top) show cytosolic eGFP (green) and
547 nuclear Hoechst Janelia 646 (magenta) in cells infected with the indicated chimeras, in the
548 presence or absence of apilimod. Quantification (bottom) shows the percentage of infected cells
549 normalized to the untreated control for each biological replicate (n = 3; shown in distinct colors).
550 Technical triplicates appear as dots of the same color. Approximately 16,000 cells were analyzed
551 per condition. Bars represent mean ± SD. Statistical significance was assessed by unpaired t test;
552 ****$P < 0.0001$. Comparisons with $P > 0.05$ are not shown.

553

554 **Figure 2. Apilimod induces dose-dependent endolysosome enlargement and inhibits VSV-**
555 **MeGFP–ZEBOV infection.**

556 **(A)** Schematic of the endolysosome enlargement assay. Vero cells not expressing TMPRSS2
557 were incubated with 10 μM Alexa Fluor 568–labeled dextran (Dextran-AF568) for 2 h, followed by
558 washes to remove unbound dextran. Cells were then treated with apilimod at the indicated
559 concentrations for 1 h and imaged live during a 30 min period, also in the presence of apilimod,
560 using 3D spinning disk confocal microscopy. Dextran-AF568 was used as a fluid-phase marker
561 of endolysosomes.

562 **(B)** Representative maximum intensity z-projection images showing Dextran-AF568 signal
563 (yellow) in cells treated with 0, 0.01, 0.05, or 5 μM apilimod. Enlarged endolysosomes are evident
564 at higher concentrations. Scale bar, 10 μm.

565 **(C)** Distribution of endolysosome radii in cells treated with increasing concentrations of apilimod.
566 Solid lines represent the mean across all cells per condition; shaded regions denote SD. Cell
567 counts: N = 24 (0 μM), 22 (0.01 μM), 29 (0.05 μM), and 24 (5 μM). The gray shaded rectangular

568 region marks the 90th percentile of endolysosome radii with a radius >0.725 μm in the control
569 group (0 μM apilimod).
570 **(D)** Percentage of endolysosomes with a radius > 0.725 μm, plotted against apilimod
571 concentration. Bars represent mean ± SD. Statistical significance was determined by one-way
572 ANOVA compared to control; ****P < 0.0001.
573 **(E)** Schematic of the infection assay. Vero cells not expressing TMPRSS2 were pretreated with
574 0, 0.005, 0.01, 0.05, or 5 μM apilimod for 1 h, followed by a 30-min infection with VSV-MeGFP–
575 ZEBOV (MOI ~ 0.5) in the continued presence of apilimod. Unbound virus was removed by three
576 washes (each containing apilimod), and cells were maintained in drug for the remainder of the
577 experiment. At 7.5 h postinfection, cells were fixed, and fraction of infected cell was determined
578 by establishing the of cells expressing MeGFP cytosolic fluorescence with respect to the total
579 number of cells identified by nuclear staining (Hoechst Janelia 646). Automated analysis was
580 performed using FIJI.
581 **(F)** Representative maximum intensity z-projections of images obtained 3D spinning disc confocal
582 fluorescence microscopy showing infected cells (MeGFP, green) and nuclei stained by Hoechst
583 Janelia 646 (magenta) for each apilimod concentration. Scale bar, 100 μm.
584 **(G)** Quantification of infection, plotted as the percentage of infected cells normalized to the
585 untreated control. Each biological replicate (n = 3) is shown in a different color; technical triplicates
586 are represented as dots of the same color. Approximately 16,000 cells were analyzed per
587 condition. Bars represent mean ± SD. Statistical significance was determined by one-way
588 ANOVA; ****P < 0.0001.
589
590 **Figure 3. Apilimod does not impair VSV-MeGFP–ZEBOV trafficking to NPC1 compartments**
591 **but blocks cytosolic escape and infection.**
592 **(A)** Schematic of the infection assay. Gene-edited SVG-A cells expressing NPC1-Halo were
593 pretreated with 5 μM apilimod for 1 h, followed by a 10-min incubation with VSV-MeGFP–ZEBOV
594 (MOI ~0.5) in the continued presence of 5 μM apilimod. Unbound virus was removed by three
595 washes (each containing 5 μM apilimod), and cells were maintained in drug for the remainder of
596 the experiment. Live-cell imaging using lattice light-sheet microscopy was performed at 50 min
597 and 4 h postinfection. Volumetric time-lapse series were acquired every 4 s for 10 min.
598 **(B, C)** Representative maximum intensity z-projections from the first frame of volumetric time
599 series acquired at 50 min postinfection in **(B)** absence (control) or presence **(C)** of 5 μM apilimod.
600 NPC1-Halo labeled with JFX 646 is shown in magenta, and VSV-MeGFP–ZEBOV in green. Scale
601 bar, 10 μm.

602 **(D)** Quantification of NPC1-positive compartments colocalizing with VSV-MeGFP–ZEBOV at 50
603 min postinfection. Each point represents a single cell (n = 22 control; n = 46 apilimod-treated).
604 Statistical significance was assessed using an unpaired t test; P > 0.05 was considered not
605 significant and is not shown.
606 **(E, F)** Representative maximum intensity z-projections from 4 h postinfection in **(E)** absence
607 **(**control**)** or presence **(F)** of 5 μM apilimod. NPC1-Halo labeled with JF 646 is shown in magenta,
608 and VSV-MeGFP–ZEBOV in green. Scale bar, 10 μm.
609 **(G)** Quantification of number of cells showing viral entry based on MeGFP signal at the nuclear
610 margin as in panel **(E).** Statistical significance was assessed by unpaired t test; ****P < 0.0001.
611
612 **Figure 4. Hypotonic stress partially inhibits VSV-eGFP–SARS-CoV-2 infection via the late**
613 **endosomal pathway but not early endosome–dependent entry.**
614 **(A**) Schematic of the infection assay. Vero cells stably expressing TMPRSS2 were pretreated for
615 1 h with 5 μM apilimod, 5 μM camostat, both, or DMSO vehicle. Cells were then incubated with
616 VSV-eGFP–SARS-CoV-2 for 30 min (MOI ~ 0.5) in the continued presence of the same treatment
617 solution. Unbound virus was removed by three washes, each containing the same treatment.
618 Cells were subsequently exposed to 0% or 60% hypotonic medium for 30 min. After treatment, 5
619 μM apilimod and 5 μM camostat were maintained in the culture medium for the remainder of the
620 experiment (Post apilimod +/- camostat). At 7.5 h postinfection, cells were fixed, and infection
621 was assessed by quantifying eGFP-positive cells relative to total nuclei (Hoechst Janelia 646
622 stain). Automated analysis was performed using FIJI.
623 **(B)** Representative maximum intensity z-projections show cytosolic eGFP (green) and nuclear
624 Hoechst Janelia 646 (magenta) under the indicated treatment conditions with apilimod or
625 camostat during virion incubation and hypotonic treatment.
626 **(C)** Quantification of infection levels. Data are shown as the percentage of infected cells
627 normalized to untreated control for each biological replicate (n = 3; shown in distinct colors).
628 Technical triplicates are represented as same-colored dots. Approximately 16,000 cells were
629 analyzed per condition. Bars represent mean ± SD. Statistical significance was determined using
630 one-way ANOVA; *P < 0.05, ****P < 0.0001. Comparisons with P > 0.05 are not shown.
631
632 **Figure 5. Cytosolic escape and infection by VSV-eGFP–G are not inhibited by apilimod.**
633 **(A)** Schematic of the infection assay. Gene-edited SVG-A cells expressing NPC1-Halo were
634 pretreated with 5 μM apilimod for 1 h, then incubated with VSV-eGFP–G (MOI ~1) for 10 min in
635 the continued presence of drug. Unbound virus was removed by three washes (each containing

636 5 μM apilimod), and cells were maintained in apilimod for the remainder of the experiment. Live-
637 cell imaging was performed at 30 min postinfection using lattice light-sheet microscopy.
638 Volumetric time-lapse series were acquired every 4 s for 10 min.
639 **(B, C)** Representative maximum intensity projections from the first (30 min) and last (40 min)
640 frames of the time series in the absence **(B)** (control) or presence **(C)** of 5 μM apilimod. NPC1-
641 Halo labeled with JFX 646 is shown in magenta, and VSV-eGFP–G in green. White arrowheads
642 mark virions localized in the cytosol. Scale bar, 10 μm.
643 **(D, E)** Quantification of cytosolic VSV-eGFP–G particles per cell at 30 and 40 min postinfection
644 in **(D)** control and **(E)** apilimod-treated cells. Lines connect values from the same cell at both time
645 points.
646 **(F)** Quantification of the percentage of VSV-eGFP–G particles in the cytosol, with or without
647 apilimod. Statistical significance was assessed by unpaired t test; $P > 0.05$ was considered not
648 significant and is not shown.
649
650 **Figure 6. Glutamine depletion moderates apilimod-induced endolysosome enlargement**
651 **and reduces its antiviral efficacy.**
652 **(A)** Schematic of the live-cell assay. Vero cells not expressing TMPRSS2 were incubated with 10
653 μM Alexa Fluor 568–labeled dextran (Dextran-AF568) for 2 h to label endolysosomes, followed
654 by washes to remove unbound dextran. Cells were then imaged live by lattice light-sheet
655 microscopy during treatment with 50 nM apilimod in either glutamine-containing or glutamine-free
656 medium. Imaging was initiated simultaneously with apilimod addition.
657 **(B)** Representative maximum intensity z-projections from volumetric time series at t = 0, 9, 21,
658 and 30 min post-apilimod addition, with or without glutamine. Dextran-AF568–labeled
659 endolysosomes are shown in yellow. Scale bar, 10 μm and 1 μm in insets.
660 **(C)** Schematic of the infection assay. Vero cells were incubated with VSV-MeGFP–ZEBOV for 30
661 min, unbound virus was removed by three washes, and cells were treated for 30 min with 50 nM
662 apilimod or DMSO vehicle in either glutamine-containing or glutamine-free medium. Cells were
663 then transferred to glutamine-containing medium with 5 μM apilimod for the remainder of the
664 experiment. At 7.5 h postinfection, cells were fixed, and infection was quantified as the percentage
665 of MeGFP-positive cells relative to total number of cells identified by nuclear staining (Hoechst
666 Janelia 646). Automated analysis was performed using FIJI.
667 **(D)** Representative maximum intensity z-projections showing infected cells (MeGFP, green) and
668 nuclei stained with Hoechst Janelia 646 (magenta) under each condition.

669 **(E)** Quantification of infection. Data are shown as the percentage of infected cells normalized to
670 untreated control. Each biological replicate (n = 3) is shown in a different color; technical triplicates
671 are represented as same-colored dots. Approximately 16,000 cells were analyzed per condition.
672 Bars represent mean ± SD. Statistical significance was assessed by unpaired t test; *P < 0.05,
673 ****P < 0.0001.
674
675 **Figure 7. Hypotonic-induced endolysosome enlargement is dose-dependent and**
676 **correlates with inhibition of VSV-MeGFP–ZEBOV infection.**
677 **(A)** Schematic of the endolysosome enlargement assay. Vero cells not expressing TMPRSS2
678 were incubated with 10 μM Alexa Fluor 568–labeled dextran (Dextran-AF568) for 2 h to label
679 endolysosomes, followed by washes to remove unbound dextran. Cells were then exposed to
680 hypotonic media (0%, 10%, 30%, or 60%) for 10 min prior to imaging, which was performed using
681 live cell spinning disk confocal microscopy. Hypotonic conditions were maintained throughout
682 image acquisition.
683 **(B)** Representative maximum intensity z-projections showing Dextran-AF568 signal (yellow) in
684 cells exposed to increasing hypotonic medium. Enlarged endolysosomes are observed in 30%
685 and 60% conditions. Scale bar, 10 μm.
686 **(C)** Distribution of endolysosome radii for cells treated with 0% (black), 10% (blue), 30% (green),
687 or 60% (red) hypotonic media. Solid lines represent the mean endolysosome radius across all
688 cells per condition; shaded areas denote SD. Cell counts: N = 24 (0%), 32 (10%), 25 (30%), and
689 27 (60%). The gray shaded region marks the 90th percentile of endolysosome with a radius >
690 0.725 μm in control cells (0%).
691 **(D)** Percentage of endolysosomes with radius >0.725 μm, plotted against hypotonic media
692 concentration. Bars represent mean ± SD. Statistical significance was assessed by one-way
693 ANOVA compared to control; **P < 0.01, ****P < 0.0001. Comparisons with P > 0.05 are not
694 shown.
695 **(E)** Schematic of the infectivity assay. Vero cells were infected with VSV-MeGFP–ZEBOV (MOI
696 ~ 0.1) for 30 min. Unbound virus was removed by three washes, and cells were then treated with
697 0%, 10%, 30%, or 60% hypotonic media or 5 μM apilimod for 30 min. Following treatment, all
698 conditions were maintained in 5 μM apilimod for the duration of the experiment. At 7.5 h
699 postinfection, cells were fixed, and infection was quantified by establishing the ratio of cells
700 expressing MeGFP cytosolic fluorescence with respect to the total number of cells identified by
701 nuclear staining using automated image analysis in FIJI.

(F) Representative maximum intensity z-projections showing infected cells (MeGFP, green) and nuclei stained with Hoechst Janelia 646 (magenta) for each treatment condition. Scale bar, 100 µm.

(G) Quantification of infection levels. Data are shown as the percentage of infected cells normalized to the untreated control for each biological replicate (n = 3; distinct colors). Technical triplicates appear as dots of the same color. Approximately 16,000 cells were analyzed per condition. Bars represent mean ± SD. Statistical significance was assessed by one-way ANOVA; ****P < 0.0001. Comparisons with P > 0.05 are not shown.

Figure 8. Hypotonic stress partially inhibits infection by VSV-eGFP–SARS-CoV-2 and VSV-MeGFP–ZEBOV, but not by VSV-eGFP–G.

(A) Schematic of the infection assay. SVG-A or Vero cells not expressing TMPRSS2 were incubated with VSV-eGFP–G, VSV-eGFP–SARS-CoV-2, or VSV-MeGFP–ZEBOV (MOI ~ 0.5) for 30 min, followed by three washes to remove unbound virus. Cells were then treated with 0% or 60% hypotonic medium for 30 min. Following treatment, cells were maintained with normal medium with either 100 nM Bafilomycin A1 (used only for VSV-eGFP–G samples) or 5 µM apilimod (used for the other virions) for the remainder of the experiment. At 7.5 h postinfection, cells were fixed, and infection was quantified by counting GFP-positive cells relative to total nuclei (Hoechst Janelia 646) using spinning disc confocal fluorescence microscopy. Automated analysis was performed in FIJI.

(B-D) Representative maximum intensity z-projection images (top) showing infected cells (eGFP, green) and nuclei (magenta) under 0% and 60% hypotonic conditions for each type of virion.

Quantification of infection levels. Data (bottom) are shown as the percentage of infected cells normalized to the untreated control for each biological replicate (n = 3; distinct colors). Technical triplicates are represented as same-colored dots. Approximately 16,000 cells were analyzed per condition. Bars represent mean ± SD. Statistical significance was assessed using an unpaired t test; ****P < 0.0001. Comparisons with P > 0.05 are not shown.

Figure 9. 3D tracking of VSV-MeGFP–ZEBOV reveals confined and membrane-bound virion populations within apilimod-induced swollen NPC1-positive endolysosomes. Associated with Movies 1-3.

(A) Schematic of the infection assay. Gene-edited SVG-A cells expressing NPC1-Halo were pretreated with 5 µM apilimod for 1 h, then incubated with VSV-MeGFP–ZEBOV (10 min, MOI ~ 1) in the continued presence of 5 µM apilimod. Unbound virus was removed by three washes

736 (each containing 5 μM apilimod), and cells were maintained in apilimod for the duration of the
737 experiment. Live-cell imaging was performed at 50 min postinfection using lattice light-sheet
738 microscopy. 3D time-lapse series were acquired every 4 s over 10 min.
739 **(B, C)** Representative 3D trajectories of individual virions moving within the lumen **(B)** or along
740 the limiting membrane **(C)** of NPC1-positive endolysosomes. NPC1-Halo–positive
741 endolysosomes are shown as light blue circles. Virion positions are color-coded by time (dark
742 blue to dark red). Insets show representative maximum-intensity z-projections from sequential
743 images of an NPC1–Halo–positive endosome labeled with JF646 (magenta) and VSV-MeGFP–
744 ZEBOV (green). Scale bar, 1 um. Mean square displacement (MSD) plots are shown; in **(B)**, the
745 radius of confinement is derived from the MSD plateau using the relationship 6/5 R^2 (inset).
746 **(D, E)** Simulated 3D trajectories reproduce the observed motion types. **(D)** Confined motion within
747 a spherical volume with step length comparable to the sphere radius. **(E)** Membrane-bound
748 motion on the surface of a rotating sphere at two rotation speeds (blue and brown). Corresponding
749 MSD curves are shown.
750 **(F)** Fraction of VSV-eGFP–G and VSV-MeGFP–ZEBOV virions exhibiting membrane-bound
751 trajectories among all virions entrapped in NPC1-positive endolysosomes. Classification was
752 based on movement patterns in 3D time-lapse maximum-intensity projections.

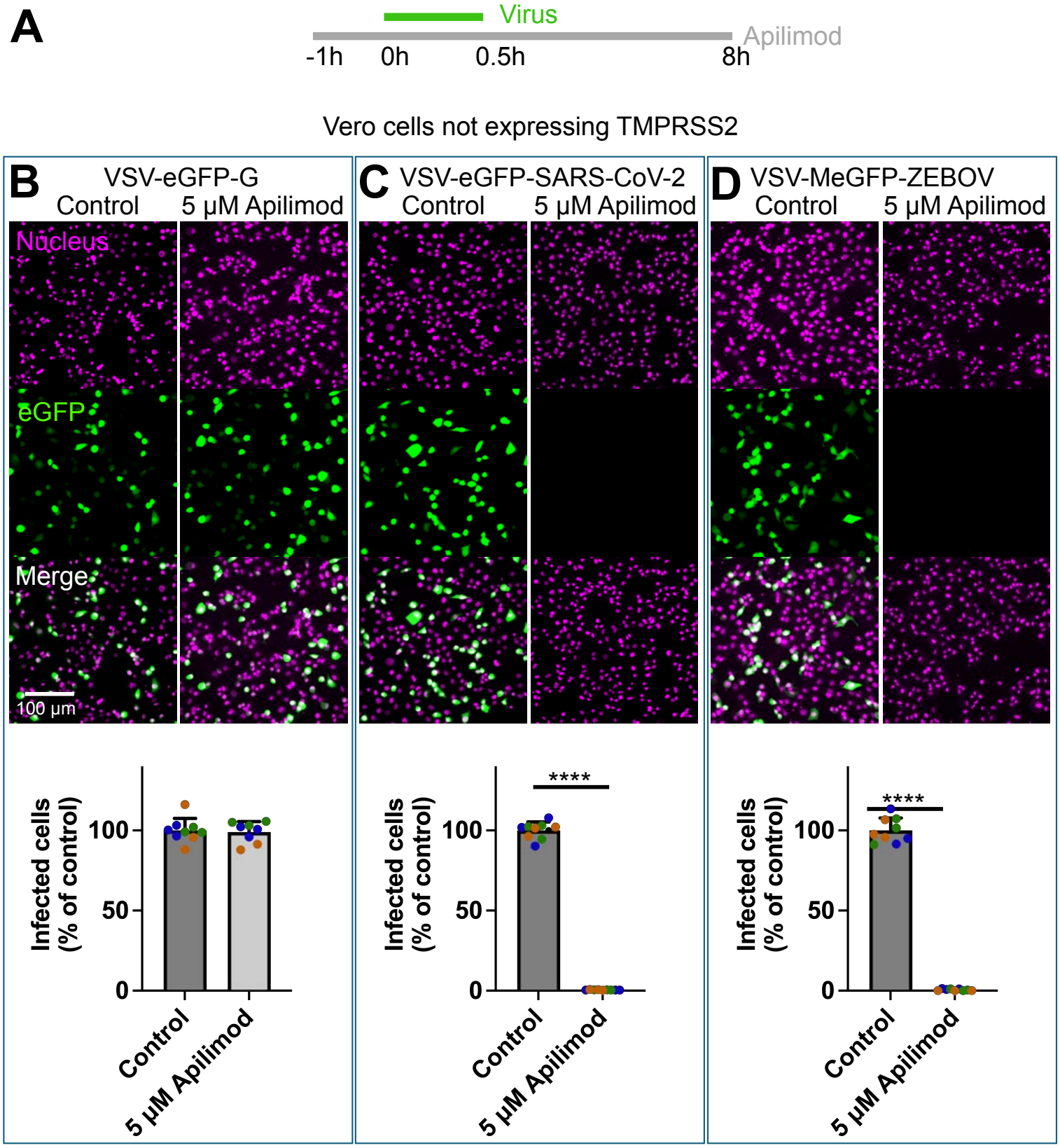
A
Virus
Apilimod
-1h
0h
0.5h
8h
Vero cells not expressing TMPRSS2
B
VSV-eGFP-G
Control
5 µM Apilimod
Nucleus
eGFP
Merge
100 µm
Infected cells (% of control)
100
50
0
Control
5 µM Apilimod
C
VSV-eGFP-SARS-CoV-2
Control
5 µM Apilimod
****
Infected cells (% of control)
100
50
0
Control
5 µM Apilimod
D
VSV-MeGFP-ZEBOV
Control
5 µM Apilimod
****
Infected cells (% of control)
100
50
0
Control
5 µM Apilimod

Figure 1

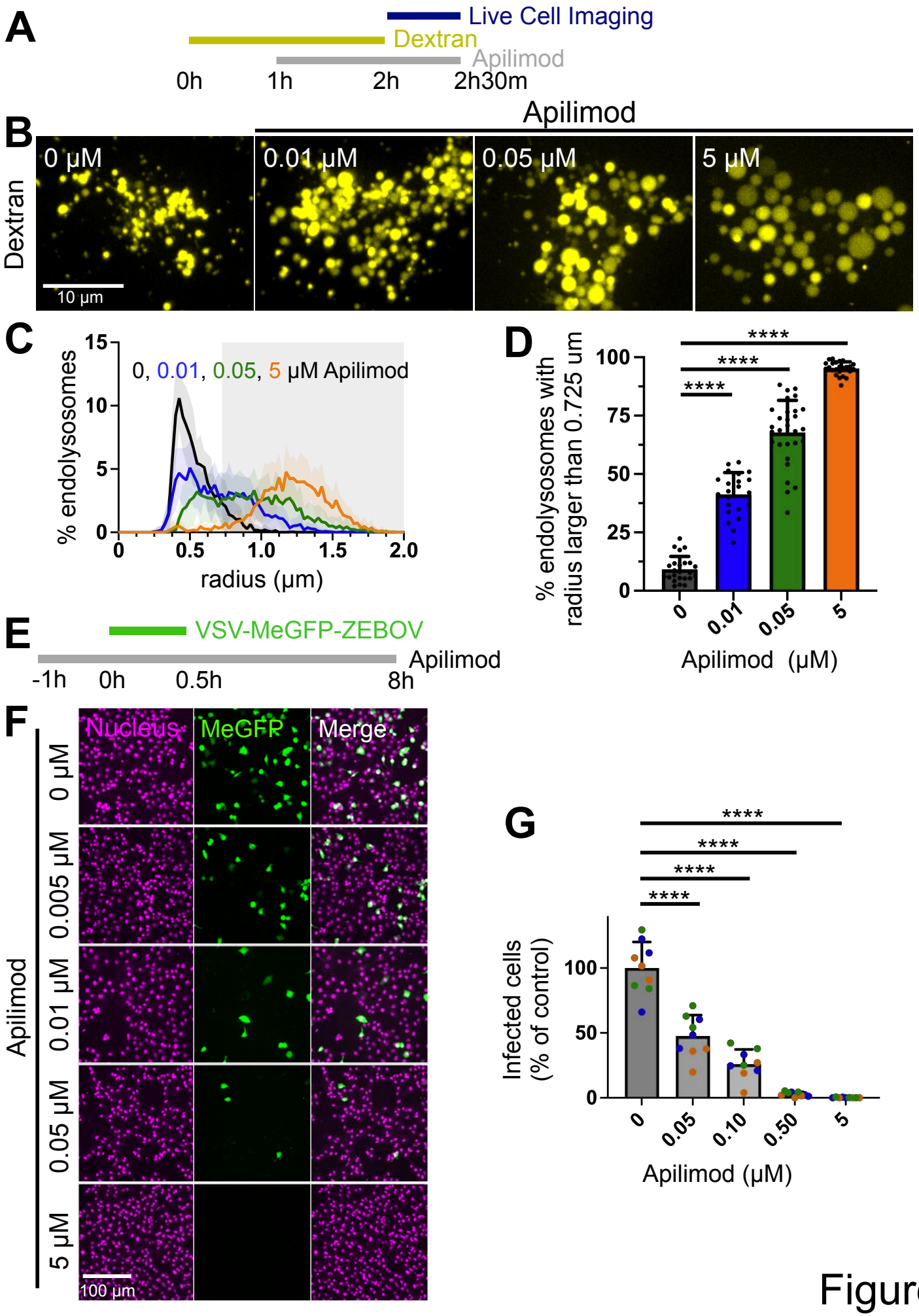
A
Live Cell Imaging
Dextran
Apilimod
0h
1h
2h
2h30m
B
Apilimod
Dextran
0 μM
0.01 μM
0.05 μM
5 μM
10 μm
C
0, 0.01, 0.05, 5 μM Apilimod
% endolysosomes
radius (μm)
D
% endolysosomes with radius larger than 0.725 um
Apilimod (μM)
E
VSV-MeGFP-ZEBOV
Apilimod
-1h
0h
0.5h
8h
F
Nucleus
MeGFP
Merge
Apilimod
0 μM
0.005 μM
0.01 μM
0.05 μM
5 μM
100 μm
G
Infected cells (% of control)
Apilimod (μM)

Figure 2

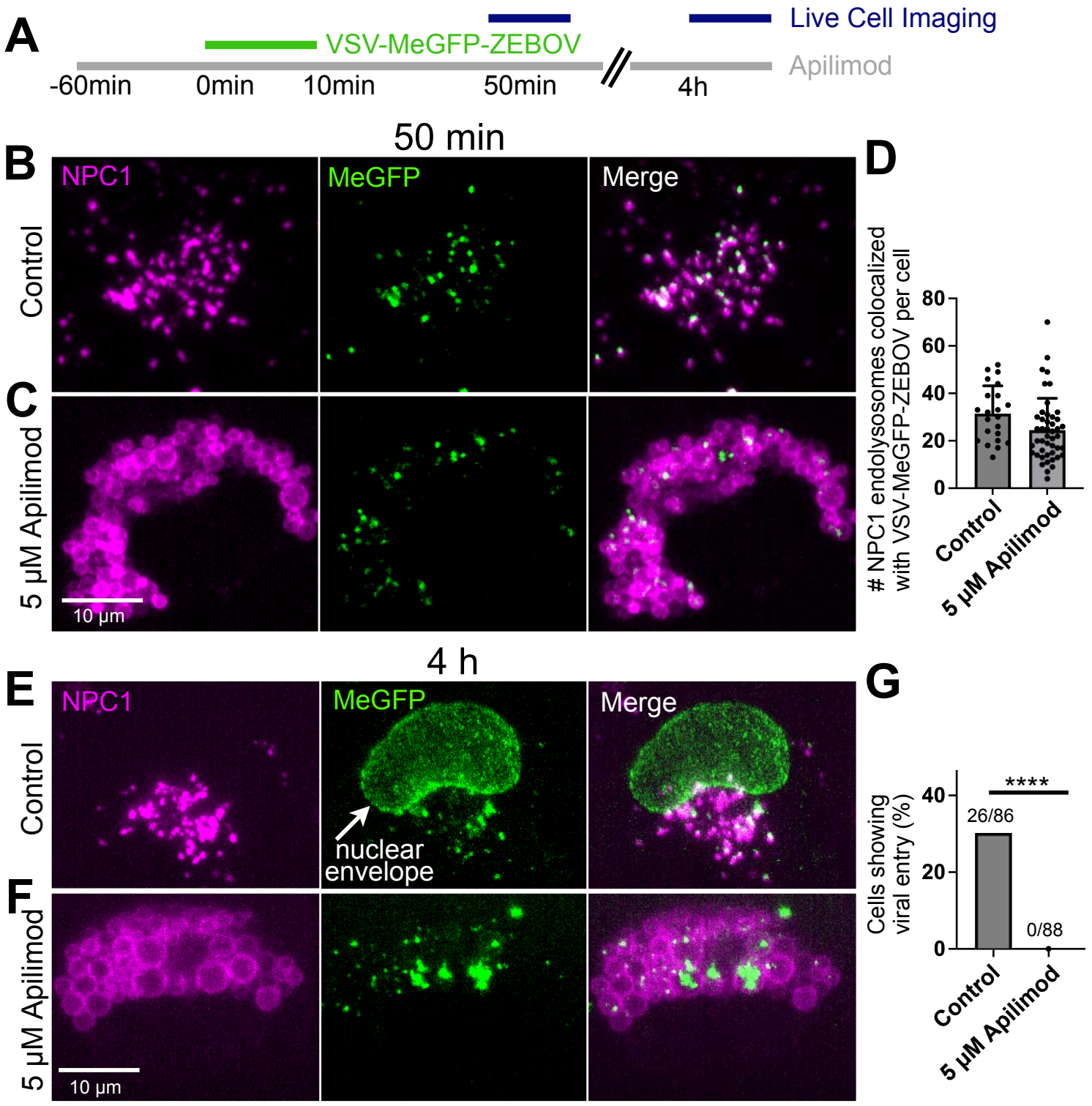
A
Live Cell Imaging
VSV-MeGFP-ZEBOV
Apilimod
-60min
0min
10min
50min
4h
50 min
B
NPC1
MeGFP
Merge
Control
C
5 µM Apilimod
10 µm
D
NPC1 endolysosomes colocalized with VSV-MeGFP-ZEBOV per cell
80
60
40
20
0
Control
5 µM Apilimod
4 h
E
NPC1
MeGFP
Merge
Control
nuclear envelope
F
5 µM Apilimod
10 µm
G
Cells showing viral entry (%)
40
20
0
****
26/86
0/88
Control
5 µM Apilimod

Figure 3

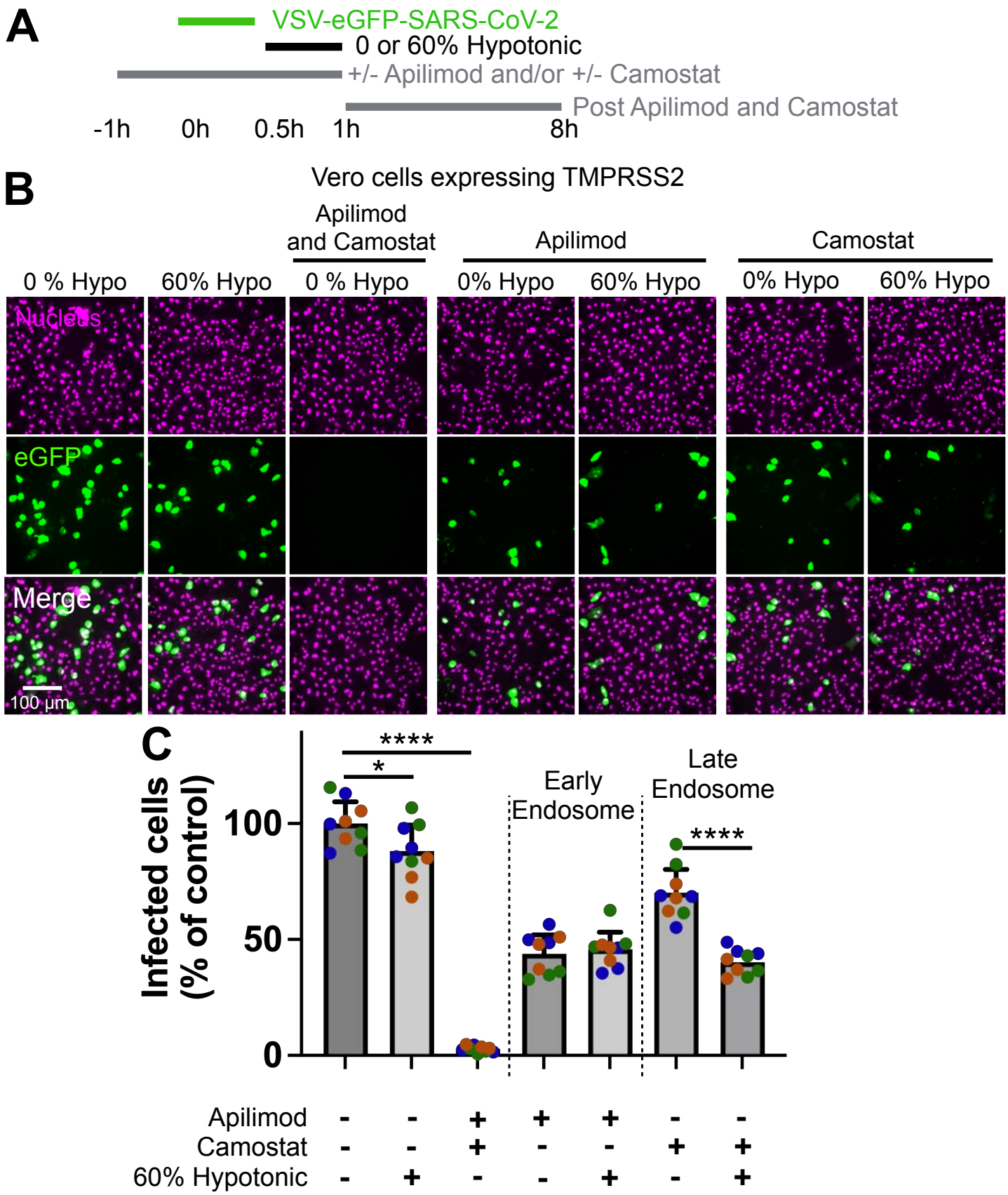
A
VSV-eGFP-SARS-CoV-2
0 or 60% Hypotonic
+/- Apilimod and/or +/- Camostat
Post Apilimod and Camostat
-1h
0h
0.5h
1h
8h
B
Vero cells expressing TMPRSS2
Apilimod and Camostat
Apilimod
Camostat
0 % Hypo
60% Hypo
0 % Hypo
0% Hypo
60% Hypo
0% Hypo
60% Hypo
Nucleus
eGFP
Merge
100 µm
C
Infected cells (% of control)
100
50
0
****
*
Early Endosome
Late Endosome
****
Apilimod - - + + + - -
Camostat - - + - - + +
60% Hypotonic - + - - + - +

Figure 4

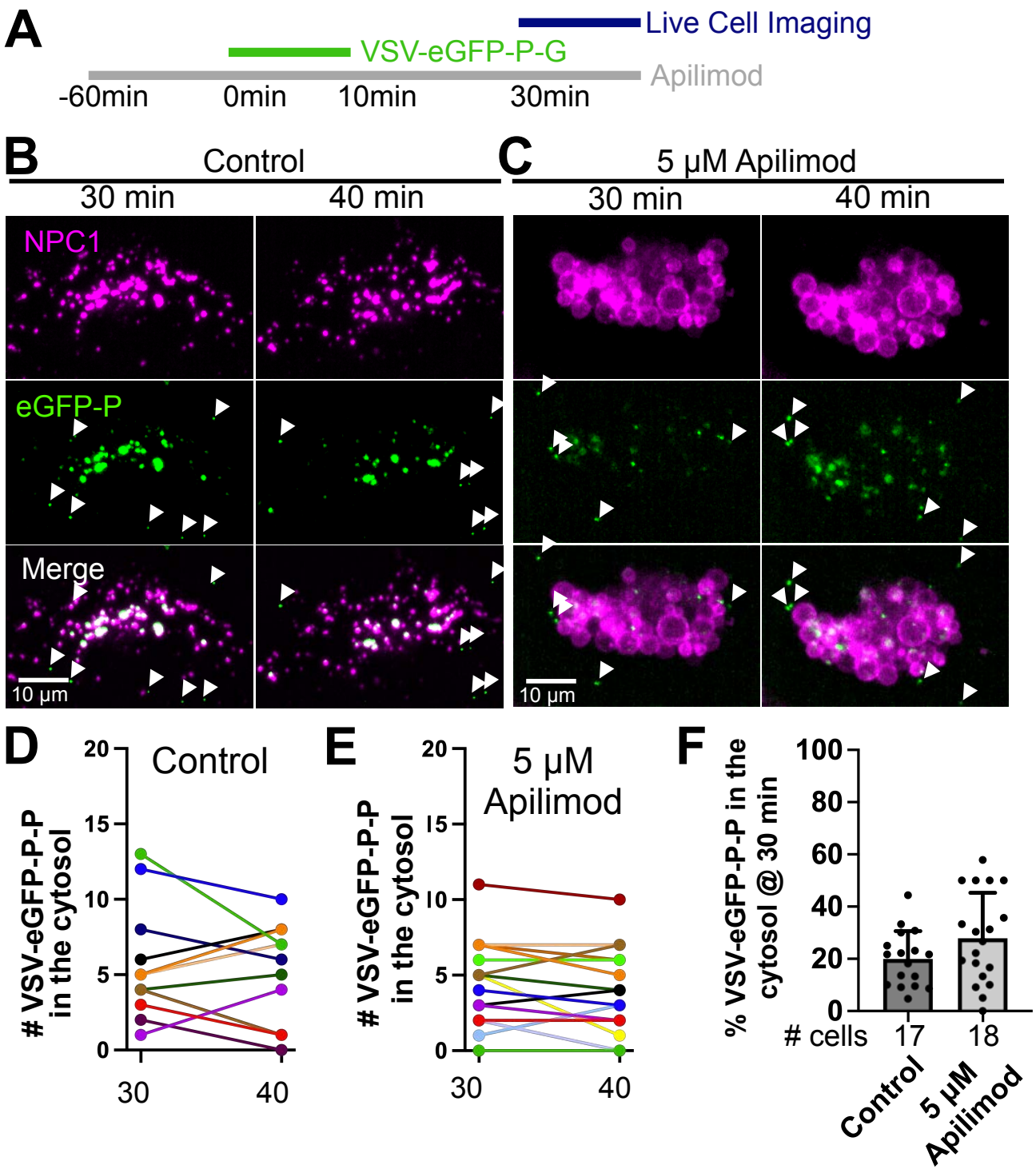
A
Live Cell Imaging
VSV-eGFP-P-G
Apilimod
-60min
0min
10min
30min
B
Control
30 min
40 min
C
5 μM Apilimod
30 min
40 min
NPC1
eGFP-P
Merge
10 μm
10 μm
D
Control
VSV-eGFP-P-P in the cytosol
E
5 μM Apilimod
VSV-eGFP-P-P in the cytosol
F
% VSV-eGFP-P-P in the cytosol @ 30 min
# cells
17
18
Control
5 μM Apilimod

Figure 5

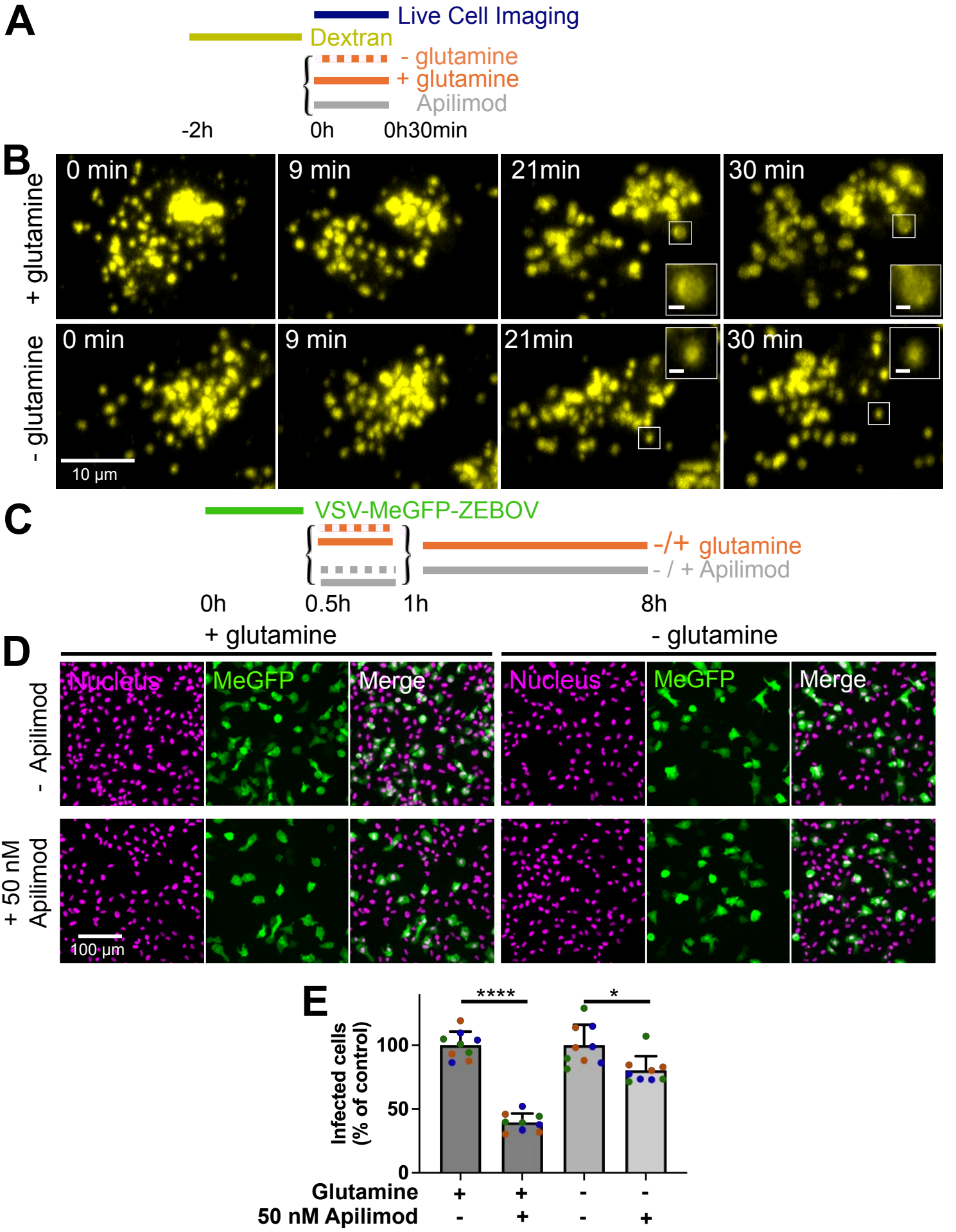
A
Live Cell Imaging
Dextran
- glutamine
+ glutamine
Apilimod
-2h
0h
0h30min
B
+ glutamine
- glutamine
0 min
9 min
21min
30 min
10 µm
C
VSV-MeGFP-ZEBOV
-/+ glutamine
- / + Apilimod
0h
0.5h
1h
8h
D
+ glutamine
- glutamine
- Apilimod
+ 50 nM Apilimod
Nucleus
MeGFP
Merge
100 µm
E
Infected cells (% of control)
100
50
0
****
*
Glutamine
50 nM Apilimod

Figure 6

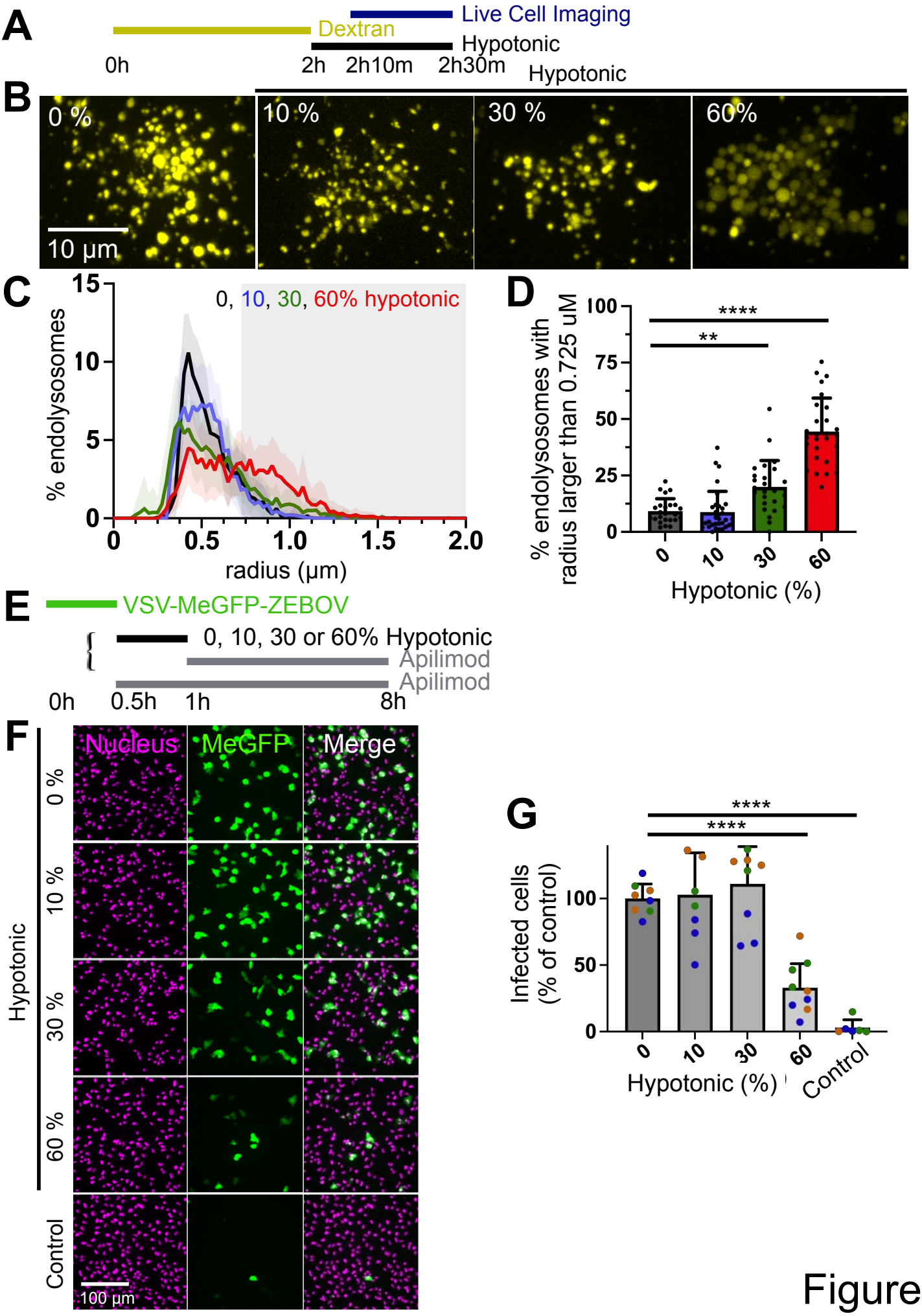
A
Live Cell Imaging
Dextran
Hypotonic
0h
2h
2h10m
2h30m
Hypotonic
B
0 %
10 %
30 %
60%
10 µm
C
0, 10, 30, 60% hypotonic
% endolysosomes
radius (µm)
D
% endolysosomes with radius larger than 0.725 uM
Hypotonic (%)
E
VSV-MeGFP-ZEBOV
0, 10, 30 or 60% Hypotonic
Apilimod
Apilimod
0h
0.5h
1h
8h
F
Nucleus
MeGFP
Merge
Hypotonic
0 %
10 %
30 %
60 %
Control
100 µm
G
Infected cells (% of control)
Hypotonic (%)
Control

Figure 7

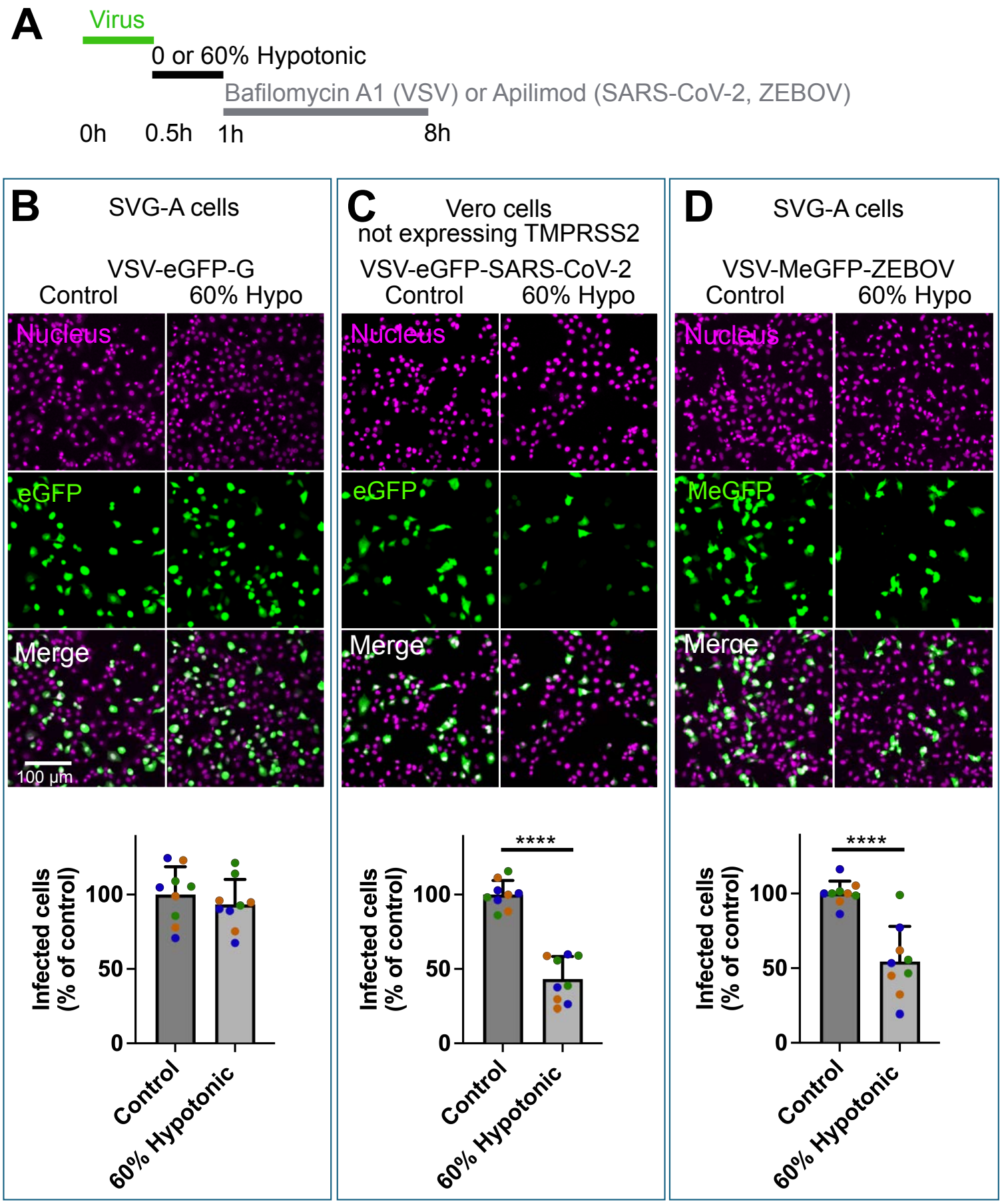
A
Virus
0 or 60% Hypotonic
Bafilomycin A1 (VSV) or Apilimod (SARS-CoV-2, ZEBOV)
0h
0.5h
1h
8h
B
SVG-A cells
VSV-eGFP-G
Control
60% Hypo
Nucleus
eGFP
Merge
100 µm
Infected cells (% of control)
100
50
0
Control
60% Hypotonic
C
Vero cells not expressing TMPRSS2
VSV-eGFP-SARS-CoV-2
Control
60% Hypo
Nucleus
eGFP
Merge
****
Infected cells (% of control)
100
50
0
Control
60% Hypotonic
D
SVG-A cells
VSV-MeGFP-ZEBOV
Control
60% Hypo
Nucleus
MeGFP
Merge
****
Infected cells (% of control)
100
50
0
Control
60% Hypotonic

Figure 8

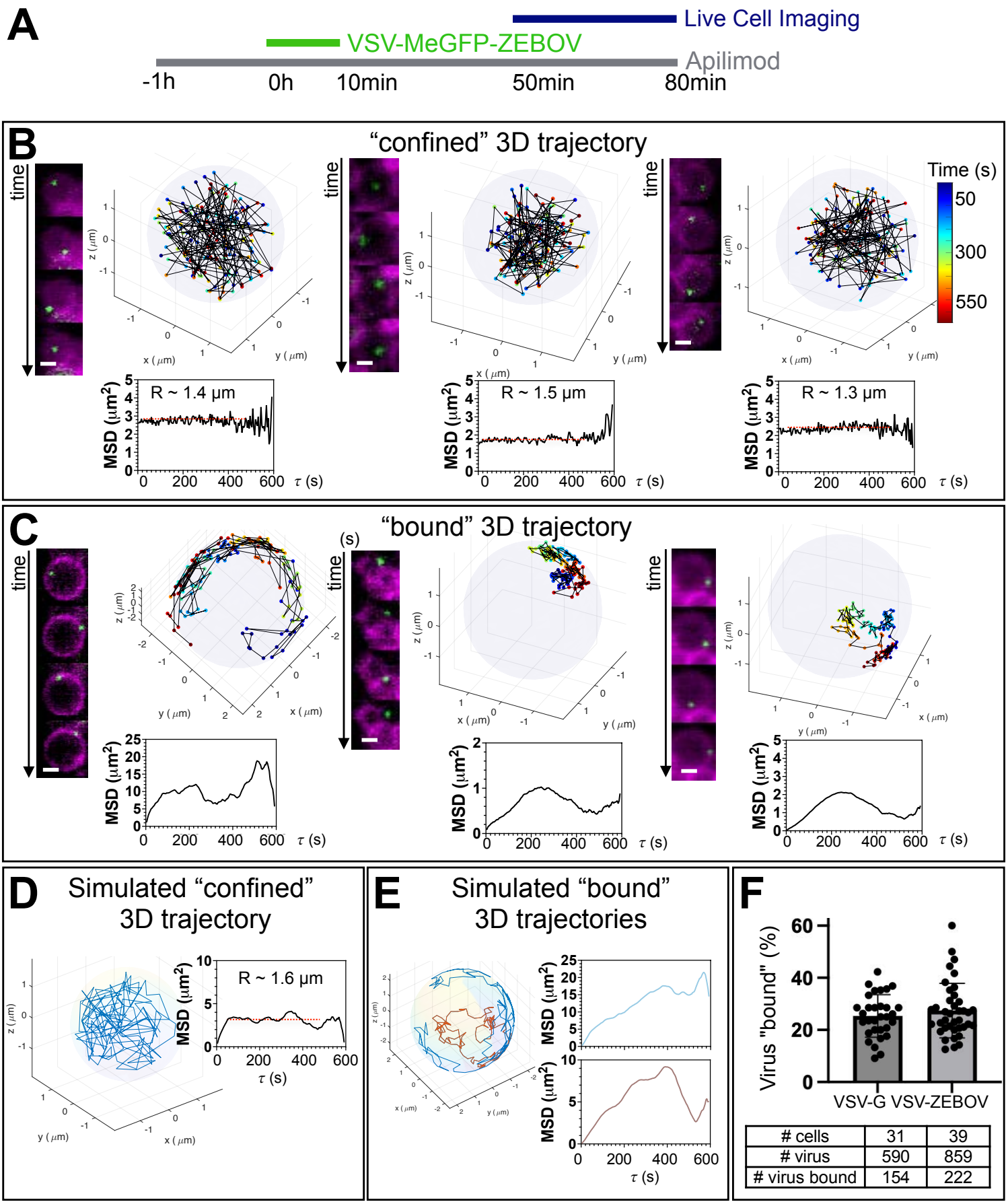
A
Live Cell Imaging
VSV-MeGFP-ZEBOV
Apilimod
-1h
0h
10min
50min
80min
B
"confined" 3D trajectory
time
Time (s)
50
300
550
R ~ 1.4 µm
R ~ 1.5 µm
R ~ 1.3 µm
MSD (µm²)
τ (s)
C
"bound" 3D trajectory
(s)
D
Simulated "confined" 3D trajectory
R ~ 1.6 µm
E
Simulated "bound" 3D trajectories
F
Virus "bound" (%)
VSV-G
VSV-ZEBOV
cells 31 39
virus 590 859
virus bound 154 222

Figure 9

753 **REFERENCES**

754 1. S. C. Harrison, Viral membrane fusion. *Virology* **479**, 498–507 (2015).

755 2. S. Belouzard, J. K. Millet, B. N. Licitra, G. R. Whittaker, Mechanisms of Coronavirus Cell Entry
756 Mediated by the Viral Spike Protein. *Viruses* **4**, 1011–1033 (2012).
757 3. H. Hofmann-Winkler, F. Kaup, S. Pöhlmann, Host Cell Factors in Filovirus Entry: Novel Players, New
758 Insights. *Viruses* **4**, 3336–3362 (2012).
759 4. J. M. White, K. L. Schornberg, A new player in the puzzle of filovirus entry. *Nat. Rev. Microbiol.* **10**,
760 317–322 (2012).
761 5. C. B. Jackson, M. Farzan, B. Chen, H. Choe, Mechanisms of SARS-CoV-2 entry into cells. *Nat Rev*
762 *Mol Cell Bio* **23**, 3–20 (2022).
763 6. S. N. Zolov, *et al.*, In vivo, Pikfyve generates PI(3,5)P2, which serves as both a signaling lipid and the
764 major precursor for PI5P. *Proc. Natl. Acad. Sci.* **109**, 17472–17477 (2012).
765 7. X. Cai, Y. Xu, Y.-M. Kim, J. Loureiro, Q. Huang, PIKfyve, a class III lipid kinase, is required for
766 TLR-induced type I IFN production via modulation of ATF3. *Journal of immunology (Baltimore, Md :*
767 *1950)* **192**, 3383–3389 (2014).
768 8. J. de Lartigue, *et al.*, PIKfyve Regulation of Endosome-Linked Pathways. *Traffic* **10**, 883–893 (2009).
769 9. J. Cerny, *et al.*, The small chemical vacuolin-1 inhibits Ca(2+)-dependent lysosomal exocytosis but not
770 cell resealing. *EMBO reports* **5**, 883–888 (2004).
771 10. O. Sano, *et al.*, Vacuolin-1 inhibits autophagy by impairing lysosomal maturation via PIKfyve
772 inhibition. *FEBS Lett.* **590**, 1576–1585 (2016).
773 11. J. H. Vines, *et al.*, A PI(3,5)P2 reporter reveals PIKfyve activity and dynamics on macropinosomes
774 and phagosomes. *J. Cell Biol.* **222**, e202209077 (2023).
775 12. E. A. Nelson, *et al.*, The phosphatidylinositol-3-phosphate 5-kinase inhibitor apilimod blocks filoviral
776 entry and infection. *PLoS Neglected Trop. Dis.* **11**, e0005540 (2017).
777 13. Y.-L. Kang, *et al.*, Inhibition of PIKfyve kinase prevents infection by Zaire ebolavirus and SARS-
778 CoV-2. *Proc National Acad Sci* **117**, 20803–20813 (2020).
779 14. Y. Seo, *et al.*, A dual inhibitor of PIP5K1C and PIKfyve prevents SARS-CoV-2 entry into cells. *Exp.*
780 *Mol. Med.* **56**, 1736–1749 (2024).
781 15. M. A. Cuesta-Geijo, *et al.*, Endosomal Maturation, Rab7 GTPase and Phosphoinositides in African
782 Swine Fever Virus Entry. *PLoS ONE* **7**, e48853 (2012).
783 16. Z. Luo, *et al.*, Inhibition of PIKFYVE kinase interferes ESCRT pathway to suppress RNA virus
784 replication. *J. Méd. Virol.* **95**, e28527 (2023).

785 17. D. H. Drewry, F. M. Potjewyd, J. L. Smith, S. Howell, A. D. Axtman, Identification of a chemical
786 probe for lipid kinase phosphatidylinositol-5-phosphate 4-kinase gamma (PI5P4Kγ). *Curr. Res. Chem.*
787 *Biol.* **3**, 100036 (2023).
788 18. J. Baker, *et al.*, Pan-antiviral effects of a PIKfyve inhibitor on respiratory virus infection in human
789 nasal epithelium and mice. *Antimicrob. Agents Chemother.* **68**, e01050-23 (2023).
790 19. H. Yang, *et al.*, LYVAC/PDZD8 is a lysosomal vacuolator. *Science* **389**, eadz0972 (2025).
791 20. I. S. Kim, *et al.*, Mechanism of membrane fusion induced by vesicular stomatitis virus G protein.
792 *Proceedings of the National Academy of Sciences* **114**, E28–E36 (2017).
793 21. T. Pathak, S. Pal, I. Banerjee, Cathepsins in cellular entry of human pathogenic viruses. *J. Virol.* **99**,
794 e01642-24 (2025).
795 22. X. Cai, *et al.*, PIKfyve, a class III PI kinase, is the target of the small molecular IL-12/IL-23 inhibitor
796 apilimod and a player in Toll-like receptor signaling. *Chem. Biol.* **20**, 912–921 (2013).
797 23. J. A. Simmons, *et al.*, Ebolavirus Glycoprotein Directs Fusion through NPC1+ Endolysosomes. *J.*
798 *Virol.* **90**, 605–610 (2015).
799 24. S. L. Winter, *et al.*, The Ebola virus VP40 matrix layer undergoes endosomal disassembly essential
800 for membrane fusion. *EMBO J.* **42**, EMBJ2023113578 (2023).
801 25. J. Koch, *et al.*, TMPRSS2 expression dictates the entry route used by SARS-CoV-2 to infect host
802 cells. *Embo J* **40**, e107821 (2021).
803 26. T. Ou, *et al.*, Hydroxychloroquine-mediated inhibition of SARS-CoV-2 entry is attenuated by
804 TMPRSS2. *Plos Pathog* **17**, e1009212 (2021).
805 27. M. Hoffmann, *et al.*, SARS-CoV-2 Cell Entry Depends on ACE2 and TMPRSS2 and Is Blocked by a
806 Clinically Proven Protease Inhibitor. *Cell* **181**, 271-280.e8 (2020).
807 28. A. J. B. Kreutzberger, *et al.*, Synergistic Block of SARS-CoV-2 Infection by Combined Drug
808 Inhibition of the Host Entry Factors PIKfyve Kinase and TMPRSS2 Protease. *J. Virol.* **95**,
809 10.1128/jvi.00975-21 (2021).
810 29. J. Uwada, *et al.*, PIKFYVE inhibition induces endosome- and lysosome-derived vacuole enlargement
811 via ammonium accumulation. *J. Cell Sci.* **138** (2025).
812 30. L. M. Compton, O. C. Ikonomov, D. Sbrissa, P. Garg, A. Shisheva, Active vacuolar H+ ATPase and
813 functional cycle of Rab5 are required for the vacuolation defect triggered by PtdIns(3,5)P2 loss under
814 PIKfyve or Vps34 deficiency. *American journal of physiology Cell physiology* **311**, C366-77 (2016).
815 31. E. Zook, *et al.*, Delayed vacuolation in mammalian cells caused by hypotonicity and ion loss. *Sci.*
816 *Rep.* **14**, 29354 (2024).
817 32. C. King, P. Sengupta, A. Y. Seo, J. Lippincott-Schwartz, ER membranes exhibit phase behavior at
818 sites of organelle contact. *Proc. Natl. Acad. Sci.* **117**, 7225–7235 (2020).

819 33. P. Li, *et al.*, LRRC8 family proteins within lysosomes regulate cellular osmoregulation and enhance
820 cell survival to multiple physiological stresses. *Proc. Natl. Acad. Sci.* **117**, 29155–29165 (2020).
821 34. A. Hazama, *et al.*, Swelling-Induced, Cftr-Independent Atp Release from a Human Epithelial Cell
822 Line. *J. Gen. Physiol.* **114**, 525–533 (1999).
823 35. E. J. Bowman, A. Siebers, K. Altendorf, Bafilomycins: a class of inhibitors of membrane ATPases
824 from microorganisms, animal cells, and plant cells. *Proc. Natl. Acad. Sci.* **85**, 7972–7976 (1988).
825 36. X. Leray, *et al.*, Tonic inhibition of the chloride/proton antiporter ClC-7 by PI(3,5)P2 is crucial for
826 lysosomal pH maintenance. *eLife* **11**, e74136 (2022).
827 37. G. Sharma, *et al.*, A family of PIKFYVE inhibitors with therapeutic potential against autophagy-
828 dependent cancer cells disrupt multiple events in lysosome homeostasis. *Autophagy* **15**, 1694–1718
829 (2019).
830 38. A. Sanyal, *et al.*, Tau seeding in neurons enabled by transient endolysosomal perforations are
831 confined within endolysosomes. *bioRxiv* (2025). https://doi.org/10.1101/2025.11.02.686178.
832 39. L. V. Chernomordik, M. M. Kozlov, PROTEIN-LIPID INTERPLAY IN FUSION AND FISSION OF
833 BIOLOGICAL MEMBRANES *. *Annu. Rev. Biochem.* **72**, 175–207 (2003).
834 40. S. C. Harrison, Viral membrane fusion. *Nat. Struct. Mol. Biol.* **15**, 690–698 (2008).
835 41. D. W. Lee, V. Thapar, P. Clancy, S. Daniel, Stochastic Fusion Simulations and Experiments Suggest
836 Passive and Active Roles of Hemagglutinin during Membrane Fusion. *Biophys. J.* **106**, 843–854 (2014).
837 42. S. Boonstra, P. R. Onck, E. van der Giessen, Computation of Hemagglutinin Free Energy Difference
838 by the Confinement Method. *J. Phys. Chem. B* **121**, 11292–11303 (2017).
839 43. V. Mercier, *et al.*, Endosomal membrane tension regulates ESCRT-III-dependent intra-lumenal
840 vesicle formation. *Nat. Cell Biol.* **22**, 947–959 (2020).
841 44. A. Colom, *et al.*, A fluorescent membrane tension probe. *Nat. Chem.* **10**, 1118–1125 (2018).
842 45. F. Piazzolla, *et al.*, Fluorescent Membrane Tension Probes for Early Endosomes. *Angew. Chem. Int.*
843 *Ed.* **60**, 12258–12263 (2021).
844 46. A. Goujon, *et al.*, Mechanosensitive Fluorescent Probes to Image Membrane Tension in
845 Mitochondria, Endoplasmic Reticulum, and Lysosomes. *J. Am. Chem. Soc.* **141**, 3380–3384 (2019).
846 47. S. R. Chadwick, *et al.*, Two-pore channels regulate endomembrane tension to enable remodeling and
847 resolution of phagolysosomes. *Proc. Natl. Acad. Sci.* **121**, e2309465121 (2024).
848 48. L. Shi, *et al.*, SNARE Proteins: One to Fuse and Three to Keep the Nascent Fusion Pore Open.
849 *Science* **335**, 1355–1359 (2012).
850 49. H. K. Johannsdottir, R. Mancini, J. Kartenbeck, L. Amato, A. Helenius, Host cell factors and
851 functions involved in vesicular stomatitis virus entry. *J Virol* **83**, 440–453 (2009).

852 50. C. E. Mire, J. M. White, M. A. Whitt, A Spatio-Temporal Analysis of Matrix Protein and
853 Nucleocapsid Trafficking during Vesicular Stomatitis Virus Uncoating. *PLoS Pathog.* **6**, e1000994
854 (2010).
855 51. S. B. Sieczkarski, G. R. Whittaker, Differential Requirements of Rab5 and Rab7 for Endocytosis of
856 Influenza and Other Enveloped Viruses. *Traffic* **4**, 333–343 (2003).
857 52. J. M. White, G. R. Whittaker, Fusion of Enveloped Viruses in Endosomes. *Traffic* **17**, 593–614
858 (2016).
859 53. R. Zang, *et al.*, TMPRSS2 and TMPRSS4 promote SARS-CoV-2 infection of human small intestinal
860 enterocytes. *Sci. Immunol.* **5**, eabc3582 (2020).
861 54. S. P. Whelan, L. A. Ball, J. N. Barr, G. T. Wertz, Efficient recovery of infectious vesicular stomatitis
862 virus entirely from cDNA clones. *Proc. Natl. Acad. Sci.* **92**, 8388–8392 (1995).
863 55. Z. Si, K. Zhou, J. Tsao, M. Luo, Z. H. Zhou, Locations and in situ structure of the polymerase
864 complex inside the virion of vesicular stomatitis virus. *Proc. Natl. Acad. Sci.* **119**, e2111948119 (2022).
865 56. J. B. Case, *et al.*, Neutralizing Antibody and Soluble ACE2 Inhibition of a Replication-Competent
866 VSV-SARS-CoV-2 and a Clinical Isolate of SARS-CoV-2. *Cell host & microbe* **28**, 475-485.e5 (2020).
867 57. A. C. Wong, R. G. Sandesara, N. Mulherkar, S. P. Whelan, K. Chandran, A forward genetic strategy
868 reveals destabilizing mutations in the Ebolavirus glycoprotein that alter its protease dependence during
869 cell entry. *Journal of virology* **84**, 163–175 (2010).
870 58. K. Zhou, *et al.*, Atomic model of vesicular stomatitis virus and mechanism of assembly. *Nat.*
871 *Commun.* **13**, 5980 (2022).
872 59. M. Arzt, *et al.*, LABKIT: Labeling and Segmentation Toolkit for Big Image Data. *Front. Comput. Sci.*
873 **4** (2022).
874 60. F. Aguet, *et al.*, Membrane dynamics of dividing cells imaged by lattice light-sheet microscopy.
875 *Molecular biology of the cell* (2016). https://doi.org/10.1091/mbc.e16-03-0164.
876 61. L. S. V. Thomas, J. Gehrig, Multi-template matching: a versatile tool for object-localization in
877 microscopy images. *BMC Bioinform.* **21**, 44 (2020).
878

879 **SUPPLEMENT**

880 **Detailed material and methods**

881 **Reagents**

882 The following reagents were used: apilimod (HY-14644, MedChemExpress), Bafilomycin A1
883 (B1793-2UG, Sigma-Aldrich), Milli-Q water (Z00QSV0US, MilliporeSigma), Minimum Essential
884 Medium (MEM; 10-010-CV, Corning), Dulbecco's Modified Eagle Medium (DMEM; 10-013-CV,
885 Corning), penicillin-streptomycin (45000-652, VWR), fetal bovine serum (S11150H, Atlanta
886 Biologicals), Alexa Fluor 568 dextran-10K (D-22912, Invitrogen), Janelia Hoechst 646 and
887 Janelia Fluor 646 HaloTag ligand (gifts from Luke Lavis, Janelia Research Campus, HHMI),
888 FluoroBrite DMEM (A1896701, Gibco), HEPES buffer (SH30237.01, Cytiva), and
889 paraformaldehyde (P6148, Sigma-Aldrich).

890

891 **Cell Culture**

892 VeroE6-TMPRSS2 cells (a gift from Siyan Ding (1)) and Vero C1008 cells (Vero 76, clone E6;
893 ATCC CRL-1586) were maintained in DMEM supplemented with 10% fetal bovine serum (FBS)
894 and 1% penicillin-streptomycin (P/S) at 37°C in 5% CO_2. SVG-A cells (ATCC CRL-8621) and a
895 homozygous gene-edited derivative expressing EEA1–mScarlet and NPC1–HaloTag from both
896 alleles (2) were cultured in MEM with 10% FBS and 1% P/S under the same conditions. All
897 experiments used cells passaged fewer than 10 times. Cultures were routinely tested and
898 confirmed negative for mycoplasma.

899

900 **Production and Propagation of Chimeric Vesicular Stomatitis Viruses**

901 Recombinant vesicular stomatitis viruses (VSVs) encoding fluorescent reporters and distinct
902 glycoproteins were used. VSV-eGFP-G expresses enhanced GFP (eGFP) and retains the
903 native VSV glycoprotein G (3). VSV-eGFP-P-G expresses eGFP fused to the viral
904 phosphoprotein (P) (2), a cofactor that associates with the large (L) polymerase protein within
905 the virion and is required for efficient RNA-dependent RNA synthesis from the ribonucleoprotein
906 (RNP) template. Each virion contains approximately 165 copies of P (4). In VSV-eGFP–SARS-
907 CoV-2, glycoprotein G is replaced by the SARS-CoV-2 spike (S) protein (Wuhan-Hu-1) (5).
908 VSV-MeGFP-ZEBOV encodes the Zaire ebolavirus (ZEBOV) glycoprotein in place of G and
909 expresses eGFP fused to the matrix (M) protein (6). We estimate that each virion contains
910 ~1200 MeGFP molecules, assuming the number of MeGFP copies approximates that of the M
911 protein in VSV (7).

912

913 Chimeric viruses were propagated in confluent Vero E6 monolayers plated in 15 cm dishes.
914 Growth medium (DMEM with 10% FBS) was removed, and cells were rinsed once with DMEM
915 containing 1% P/S to remove residual serum. Cells were infected at a multiplicity of infection
916 (MOI) of ~0.01 in 10 mL DMEM supplemented with 0.4% FBS and 1% P/S and incubated for 48
917 h at 37°C, 5% CO_2. Supernatants were collected, clarified by centrifugation at 3580 rpm for 10
918 min at 4°C (Beckman Coulter GS-6KR), and divided into two portions: one was stored at 4°C for
919 up to one week for titration and infection assays; the other was aliquoted (0.5 mL), flash-frozen
920 in liquid nitrogen, and stored at −80°C for imaging-based experiments.
921
922 **Virus infection**
923 Viral supernatant (100 µL) was diluted in serum-free DMEM containing 1% P/S and applied to
924 cells plated in 48-well plates (82051-004, VWR) for 30 min at 37°C. Unbound virus was
925 removed by three washes with DMEM supplemented with 10% FBS and 1% P/S. Cells were
926 then incubated in fresh complete medium for 8 h at 37°C in 5% CO_2. Fixation was performed
927 with 4% paraformaldehyde (PFA) in PBS for 15 min at room temperature. The multiplicity of
928 infection (MOI) was estimated by quantifying eGFP-positive cells relative to the total population
929 (see Infection Analysis). The 16% (w/v) stock PFA solution was prepared by dissolving 16 g of
930 PFA powder (P6148, Sigma-Aldrich) in 80 mL of preheated 1× PBS (60°C) with stirring for 10
931 min. We added drops of 10 N NaOH (221465, Sigma-Aldrich) every 5 min until the suspension
932 cleared. After cooling to room temperature, we filtered the solution through a grade 1
933 Whatman™ filter (09-805-1G, Cytiva), adjusted the pH to 7.2 using a calibrated pH meter (Hi
934 2211, Hanna Instruments), and aliquoted it into 10 mL portions for storage at −20°C.
935
936 **Apilimod Treatment and Infection**
937 Vero E6 cells were seeded at 35–40% confluency in sterile 48-well plates (82051-004, VWR)
938 and used the following day. Cells were pretreated for 1 h at 37°C with 0.1% dimethyl sulfoxide
939 (DMSO; vehicle control) or with 0.01, 0.05, or 5 µM apilimod in DMEM supplemented with 10%
940 FBS and 1% P/S. After pretreatment, cells were inoculated with the indicated chimeric virus for
941 30 min in serum-free DMEM containing 1% P/S and the corresponding concentration of DMSO
942 or apilimod. Unbound virus was removed by three washes with DMEM containing 10% FBS and
943 1% P/S, followed by incubation for 7 h at 37°C in 5% CO_2. Cells were then washed three times
944 with PBS (0.5 mL) and fixed with 4% PFA in PBS for 15 min at room temperature. Nuclei were
945 labeled by incubation with 100 nM Janelia Hoechst 646 in PBS for 1 h at room temperature.
946 Imaging was performed without washing out the dye.

947

948 **Hypotonic treatment and Infection**

949 Hypotonic media were prepared by diluting complete MEM or DMEM with sterile Milli-Q water:
950 10% (1 mL water + 9 mL medium), 30% (3 mL water + 7 mL medium), and 60% (6 mL water + 4
951 mL medium).

952

953 SVG-A or Vero E6 cells were seeded at 35–40% confluency in 48-well plates and used the
954 following day. Cells were infected VSV-eGFP–SARS-CoV-2 or VSV-MeGFP-ZEBOV at an MOI
955 of ~0.5 for 30 min in 200 µL of serum-free MEM for SVG-A or DMEM for Vero E6, each
956 supplemented with 1% P/S, at 37°C and 5% CO_2. Unbound virus was removed by three washes
957 with complete medium (MEM or DMEM supplemented with 10% FBS and 1% P/S, 0.5 mL per
958 wash). Infection was then either blocked by adding 100 nM bafilomycin A1 (VSV-eGFP) or 5 µM
959 apilimod (VSV-eGFP–SARS-CoV-2 and VSV-MeGFP-ZEBOV), and allowed to proceed in
960 corresponding serum-free or hypotonic media for 30 min at 37°C. Cells were then returned to
961 complete medium (10% FBS, 1% P/S) and incubated for 7 h at 37°C in 5% CO_2.

962

963 Vero cells stably expressing TMPRSS2 were seeded at 35–40% confluency in sterile 48-well
964 plates (82051-004, VWR) and used the next day. Cells were pretreated for 1 h at 37°C in 5%
965 CO_2 with 0.1% DMSO (vehicle) alone or with 5 µM apilimod, 5 µM camostat, or both in DMEM
966 supplemented with 10% FBS and 1% P/S. Following pretreatment, cells were infected with
967 VSV-eGFP-SARS-CoV-2 (MOI ~0.5) in 200 µL serum-free DMEM (1% P/S) containing the
968 same inhibitor conditions. After 30 min at 37°C, unbound virus was removed by three washes
969 with complete DMEM (10% FBS, 1% P/S; 0.5 mL/wash). Infection was then allowed to proceed
970 for 30 min in 60% hypotonic medium containing 0.1% DMSO alone or with 5 µM apilimod, 5 µM
971 camostat, or both. Cells were subsequently returned to complete DMEM containing the same
972 inhibitor conditions to prevent further infection and incubated for 7 h at 37°C in 5% CO_2.

973

974 The experiment ended by washing the cells three times with PBS (0.5 mL), fixing with 4% PFA
975 in PBS for 15 min at room temperature, and staining with 500 nM Janelia Hoechst 646 in PBS
976 for 1 h before imaging.

977

978 **Glutamine Deficiency and Infection**

979 SVG-A cells were seeded at 35–40% confluency in sterile 48-well plates (82051-004, VWR) and
980 used the next day. Cells were infected with the VSV-MeGFP-ZEBOV chimeric virus (MOI ~0.5)

981 for 30 min in serum-free DMEM (including 4 mM glutamine) supplemented with 1% P/S.
982 Unbound virus was removed by three washes with FluoroBrite DMEM supplemented with 10%
983 FBS, 1% P/S (glutamine-free) or DMEM (including 4 mM glutamine) supplemented with 10%
984 FBS and 1% P/S . The cells were incubated in FluoroBrite DMEM (glutamine-free, 10% FBS,
985 1% P/S) or DMEM (4 mM glutamine,10% FBS, 1% P/S) containing either 0.1% DMSO or 50 nM
986 apilimod for 30 min at 37°C. After three washes with DMEM (including 4 mM glutamine)
987 supplemented with 10% FBS and 1% P/S, cells were incubated for 7 h at 37°C in 5% CO_2, then
988 washed three times with PBS (0.5 mL) and fixed with 4% PFA in PBS for 15 min at room
989 temperature. Nuclei were then labeled by incubating cells with 100 nM Hoechst Janelia 646 in
990 PBS for 1 h at room temperature. Imaging was performed without washing out Hoechst Janelia
991 646 dye.
992
993 **Apilimod, Glutamine, and Hypotonic Treatments and Endolysosomal Size**
994 Vero E6 cells were seeded at 35–40% confluency in 8-well glass-bottom chambers (C8-1.5H-N,
995 Cellvis) and imaged the following day. Endolysosomes were labeled by incubating cells with 10
996 μM Alexa Fluor 568–dextran in DMEM supplemented with 10% FBS and 1% P/S for 2 h at 37°C
997 in 5% CO_2. Apilimod (final concentration of 0.01, 0.05 or 5 μM in 0.1 % DMSO) was added for 1
998 h before and then during the Dextran uptake period, after which cells were washed three times
999 with complete DMEM media (supplemented with 10% FBS and 1% P/S) to remove extracellular
1000 dye, followed by live cell imaging in FluoroBrite DMEM supplemented with 5% FBS, 1% P/S,
1001 and 25 mM HEPES (pH 7.2) including apilimod at the indicated concentrations. Experimental
1002 conditions were initiated in 15-minute intervals across the 8-well chamber. Each well was
1003 imaged for 10 minutes before applying the same washing and medium exchange protocol to the
1004 next well.
1005
1006 To study the effect of glutamine removal on apilimod induced endolysosome expansion, SVG-A
1007 cells were seeded at 35-40% confluency in 8-well glass bottom chambers (C8-1.5H-N, Cellvis)
1008 for the following day. Endolysosomes were pre-labeled with 10 μM Alexa Fluor 568–dextran in
1009 DMEM supplemented with 10% FBS and 1% P/S for 2 h at 37°C in 5% CO_2. Prior imaging,
1010 media was replaced with 50 nM of apilimod in FluoroBrite DMEM supplemented with 10% FBS,
1011 1% P/S (glutamine-free) or DMEM supplemented with 10% FBS and 1% P/S, (including 4 mM
1012 glutamine). and timelapse images were acquired in lattice light sheet microscopy to record
1013 apilimod induced expansion of dextran labeled compartments.
1014

1015 For osmotic expansion assays, we replaced the imaging medium with hypotonic solutions (10%,
1016 30%, or 60%) and immediately initiated live-cell imaging on a spinning disk confocal microscope
1017 at 2-minute intervals for 30 minutes.
1018
1019 **Virus Tracking**
1020 Gene-edited SVG-A cells expressing EEA1–mScarlet and NPC1–HaloTag chimeras instead of
1021 the native proteins were seeded at 35–40% confluency in 8-well glass-bottom chambers and
1022 imaged the following day. NPC1 compartments were labeled by incubating cells with 500 nM
1023 Janelia Fluor 646 HaloTag ligand (JFX 646) in MEM supplemented with 10% FBS and 1% P/S
1024 for 15 min at 37°C, followed by three washes with the same medium.
1025
1026 Cells were then pretreated for 1 h with 0.1% DMSO (vehicle) or 5 μM apilimod in complete
1027 MEM. After pretreatment, cells were incubated with the indicated virus in the same medium for
1028 10 min at 37°C, washed three times, and returned to fresh medium containing the same drug
1029 conditions for an additional 50 min. Live 3D imaging was performed using a lattice light-sheet
1030 microscope in FluoroBrite DMEM supplemented with 5% FBS, 1% P/S, 25 mM HEPES (pH
1031 7.2), 0.1% DMSO, and 5 μM apilimod.
1032
1033 **Fluorescence Microscopy**
1034 **Imaging of Fixed Samples to Assess Primary Infection**
1035 Fixed-cell imaging was performed using a Zeiss Axiovert 200M inverted microscope (Carl Zeiss)
1036 equipped with a CSU-22 spinning disk confocal unit (Yokogawa) and controlled by the Marianas
1037 imaging platform (3i, Intelligent Imaging Innovations). A 10× objective with a 2× magnifier was
1038 used. Samples were excited with 491 nm and 660 nm solid-state lasers (50 mW each), and
1039 fluorescence was detected using 525/50 and 680LP emission filters (Semrock), respectively.
1040
1041 Z-stacks (12 optical sections at 3 μm intervals) were acquired with a piezoelectric Z-stage (PZ-
1042 2000) and encoded XY stage (MS-2000, Applied Scientific Instruments). Images were captured
1043 at 50% laser power (0.68 mW at the back aperture) with 200 ms exposure per plane using a
1044 QuantEM 512SC air-cooled CCD camera (Photometrics).
1045
1046 **Live-Cell 3D Imaging of Endosomes and Lysosomes**
1047 Live imaging was performed using a Zeiss Axio Observer Z1 inverted microscope equipped with
1048 environmental control (37°C, 5% CO_2) and a CSU-X1 spinning disk confocal unit (Yokogawa),

1049 operated via the Marianas (3i) platform. The system included a spherical aberration correction
1050 module and a 3i LaserStack with diode lasers at 488, 560 (150 mW), and 640 nm (100 mW).
1051 Emission was filtered using 525/40, 609/54, and 692/40 filters (Semrock).
1052
1053 Z-stacks comprising 75 optical planes at 0.270 µm spacing were acquired with 20 ms exposure
1054 per plane using a dual-camera sCMOS system (Prime 95B, Teledyne Photometrics). A custom
1055 bandpass dichroic (Semrock; transmit 350–560 nm and 641–800 nm, reflect 561–640 nm)
1056 enabled simultaneous multichannel imaging. Final XY resolution was 0.145 × 0.145 µm/pixel.
1057
1058 **Live-Cell 3D Lattice Light Sheet Microscopy for Virus Tracking**
1059 Lattice light sheet imaging was performed using a Zeiss Lattice Lightsheet 7 system with a
1060 dithered lattice beam (30 µm × 0.7 µm). Cells were maintained at 37°C in a humidified chamber
1061 with 5% CO_2. Illumination was provided by 488 nm (10 mW, 2 mW at pupil), 561 nm (10 mW, 2
1062 mW), or 640 nm (5 mW, 1 mW) lasers, typically operated at 1–1.5% power.
1063
1064 A 13.3×, NA 0.4 objective (Zeiss) was used for illumination, and a 44.83×, NA 1.0 objective
1065 (Zeiss) for detection. Z-stacks were acquired using sample scanning with 0.25 µm optical
1066 sectioning and 0.5 µm axial spacing. Each plane was captured with a 5 ms exposure using dual
1067 ORCA-Fusion sCMOS cameras (Hamamatsu), yielding a final XY resolution of 0.145 × 0.145
1068 µm/pixel.
1069
1070 Time-lapse imaging was performed at 3 s intervals for virus tracking and at 3 min intervals for
1071 apilimod-induced endosome and lysosome expansion, over durations of 5–45 min. Raw image
1072 stacks were deskewed using ZEISS ZEN 3.11 software prior to analysis.
1073
1074 **Image Analysis**
1075 ***Infectivity assay***
1076 Z-stacks (12 optical sections) were acquired at 20× magnification to capture cytosolic eGFP
1077 signal from infected cells and nuclear staining with Hoechst 646, imaged 8 h post-inoculation
1078 (see Fluorescence Microscopy). This protocol ensured that the signal reflected a single round of
1079 infection (2). Maximum intensity projections were generated using FIJI. Nuclear segmentation
1080 was performed using the LabKit plugin in FIJI (8) to determine the number of cells per field and
1081 to generate nuclear masks for infection scoring.
1082

1083 A cell was classified as infected if the eGFP signal within the nuclear mask (z-maximum
1084 projection) exceeded a threshold defined by the signal in the eGFP channel from uninfected
1085 control samples. The percentage of infected cells was calculated as the number of eGFP-
1086 positive nuclei relative to the total number of segmented nuclei, using a custom FIJI script.
1087 Results were validated by visual inspection of a representative subset. A minimum of 16,000
1088 cells per condition were analyzed, derived from three independent experiments, each performed
1089 in triplicate.
1090

1091 **Colocalization Between NPC1–Halo–Labeled Compartments and Fluorescently Tagged**
1092 **Virions**

1093 Z-stacks from single-timepoint live-cell 3D lattice light sheet images of cells inoculated with M–
1094 eGFP–tagged virions were used to assess colocalization with NPC1–Halo–labeled
1095 endolysosomal compartments. Virus particles, detected as diffraction-limited spots, were
1096 identified using the MATLAB-based 3D CME Analysis software (9). For each virion, mean
1097 fluorescence intensity in the NPC1–Halo channel was measured in a 3 × 3 × 3 voxel cube
1098 centered on the particle. A virion was classified as colocalized if the NPC1–Halo signal within
1099 this volume exceeded the background signal measured in a cytosolic region devoid of NPC1–
1100 Halo signal. Analysis was automated using a custom MATLAB script and manually validated in
1101 FIJI.
1102

1103 **Measurement of Endosome and Lysosome Radii**

1104 Endosomes and lysosomes labeled with Alexa Fluor 568–dextran internalized for 2 hr were
1105 imaged volumetrically using 3D live-cell spinning disk confocal microscopy. Centroid positions of
1106 labeled compartments were identified using the 3D CME Analysis software (9). At the z-plane
1107 corresponding to each centroid, radial intensity profiles were calculated in the XY plane by
1108 measuring the distance from the centroid to the point at which fluorescence intensity declined to
1109 30% of the peak value. Measurements were taken in 2° increments over 360° (180
1110 measurements per compartment), and the mean radial distance was reported as the organelle
1111 radius.
1112

1113 **3D Tracking of Virions Within NPC1–Halo–Labeled Endolysosomes**

1114 Live-cell 3D time-lapse datasets acquired using lattice light sheet microscopy were used to track
1115 the motion of M–eGFP–tagged virions within apilimod-induced swollen endolysosomes labeled
1116 with NPC1–Halo. The centroid and fluorescence intensity of each diffraction-limited virion were

determined at each time point using the 3D CME Analysis software (9). Virion trajectories were assembled by linking detections across frames based on two criteria:

(i) The virion remained within a 3D spatial window centered on an NPC1–Halo–positive endolysosome, defined in XY as a 25 × 25-pixel region (~2.5 × 2.5 μm), centered on the centroid position of the compartment identified using the Multi-Template Matching plugin in FIJI (10) . The Z-position of the endolysosome centroid was assigned as the plane of maximal NPC1–Halo signal within ±4 z-planes.

(ii) The virion's fluorescence intensity varied by no more than ± 30% between consecutive time points.

We computed the mean square displacement (MSD) from time series of 3D centroid positions for each virion associated with an enlarged endosome. For each trajectory, we calculated the time-averaged squared displacement as a function of lag time. We classified motility by the lag-time dependence of the MSD. Confined motion showed a brief initial rise followed by a plateau, as confirmed by simulation. In contrast, virions bound to structural elements within the enlarged endosome (e.g., the limiting membrane) lacked a plateau and, after the initial rise, exhibited broad variation in MSD with lag time. Simulations show that rotation of the enlarged endosome accounts for this broad variation.

Confinement of a trajectory within a given endolysosome was validated by visual inspection in FIJI, using maximum intensity projections overlaid with bounding boxes centered on the XY coordinates of the NPC1–Halo signal.

1139 **Fig. S1. Apilimod fails to induce swelling of early endosomes EEA1-positive/NPC1-**
1140 **negative compartments (Related to Fig. 3).**
1141 **(A)** Schematic of live cell imaging experiment. Gene-edited SVG-A cells expressing NPC1-Halo
1142 labeled with JFX 646 and EEA1-mScarlet were pretreated with 5 μM apilimod for 1 h and
1143 imaged live during a 10 min period, also in the presence of apilimod, using lattice light-sheet
1144 microscopy.
1145 **(B, C)** Representative maximum intensity z-projections in the absence (control **(B)**) or presence
1146 **(C)** of 5 μM apilimod. NPC1-Halo labeled with JFX 646 is shown in magenta, and EEA1-
1147 mScarlet in cyan. White arrowheads indicate early endosomes (EEA1-positive/NPC1-negative).
1148 Scale bar, 10 μm.
1149 **(C)** Top panel presents EEA1 images with higher contrast to visualize dimmer early endosomes;
1150 bottom panel presents the image in the same contrast as control **(B)**.
1151 **(D)** Schematic of the live-cell imaging experiment. Gene-edited SVG-A cells expressing NPC1–
1152 Halo (labeled with JFX646) and EEA1–mScarlet were pretreated with 5 μM apilimod for 30 min
1153 and imaged live by lattice light-sheet microscopy for 10 min in the continued presence of
1154 apilimod, under normal conditions or during incubation in 60% hypotonic medium (initiated 20
1155 min before imaging and maintained throughout imaging).
1156 **(E)** Representative single plane images in absence or presence of 5 μM apilimod or 60%
1157 hypotonic media. NPC1-Halo labeled with JFX 646 is shown in magenta, and EEA1-mScarlet in
1158 cyan. Scale bar, 10 μm.
1159
1160 **Fig. S2. 3D tracking of VSV-MeGFP–ZEBOV reveals confined virion populations within**
1161 **apilimod-induced swollen NPC1-positive endolysosomes. Associated with Fig 9 and**
1162 **Movies 1-3.**
1163 **(A)** Schematic of the infection assay. Gene-edited SVG-A cells expressing NPC1-Halo were
1164 pretreated with 5 μM apilimod for 1 h, then incubated with VSV-MeGFP–ZEBOV (10 min, MOI ~
1165 1) in the continued presence of 5 μM apilimod. Unbound virus was removed by three washes
1166 (each containing 5 μM apilimod), and cells were maintained in apilimod for the duration of the
1167 experiment. Live-cell imaging was performed at 50 min postinfection using lattice light-sheet
1168 microscopy. 3D time-lapse series were acquired every 4 s over 10 min.
1169 **(B, C)** Representative 3D trajectories of individual virions moving within the lumen **(B)** or along
1170 the limiting membrane **(C)** of NPC1-positive endolysosomes. NPC1-Halo–positive
1171 endolysosomes are shown as light blue circles. Virion positions are color-coded by time (dark
1172 blue to dark red). Insets show representative maximum-intensity z-projections from sequential

1173 images of an NPC1–Halo–positive endosome labeled with JF646 (magenta) and VSV-MeGFP–
1174 ZEBOV (green). Scale bar, 1 um. Mean square displacement (MSD) plots are shown; in **(B)**, the
1175 radius of confinement is derived from the MSD plateau using the relationship 6/5 R^2 (inset).
1176
1177 **Movies 1–3. Associated to Fig. 9 B and C.** Live-cell 3D time-lapse imaging of VSV-MeGFP–
1178 ZEBOV virions (green) associated with endolysosomes enlarged by PIKfyve inhibition with
1179 apilimod. SVG-A cells expressing gene-edited NPC1–Halo labeled with JF 646 (magenta). Cells
1180 were pretreated with 5 μM apilimod for 1 h and then incubated with fluorescent VSV-MeGFP–
1181 ZEBOV (10 min, MOI ~1) in the continued presence of apilimod. Live-cell imaging by LLSM was
1182 performed 50 min postinfection. The 3D time-lapse series, acquired every 4 s for 10 min, are
1183 displayed as maximum-intensity projections. Scale bar, 2 μm.

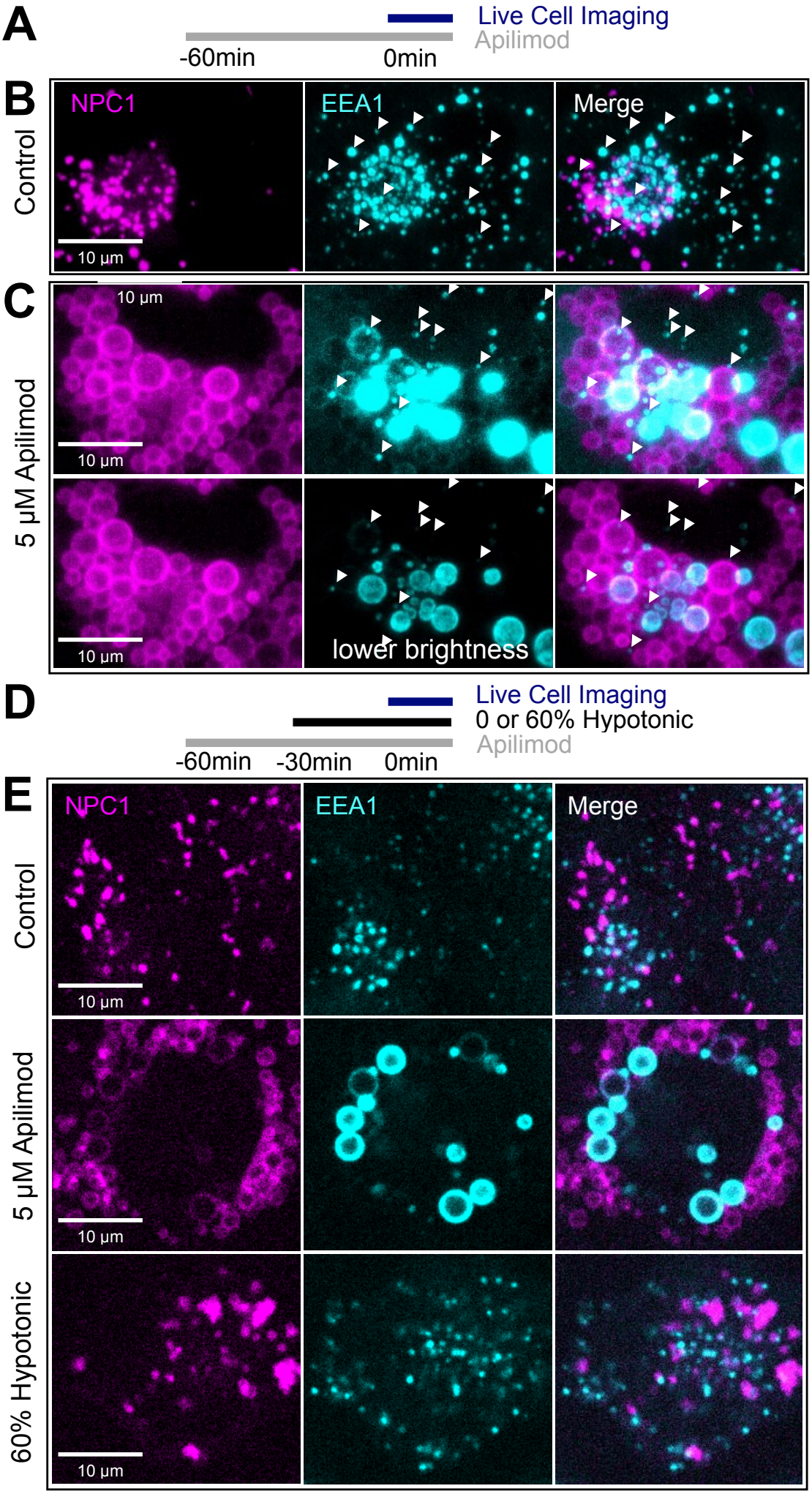
A
Live Cell Imaging
Apilimod
-60min
0min
B
Control
NPC1
EEA1
Merge
10 µm
C
5 µM Apilimod
10 µm
lower brightness
D
Live Cell Imaging
0 or 60% Hypotonic
Apilimod
-60min
-30min
0min
E
Control
5 µM Apilimod
60% Hypotonic

Figure S1

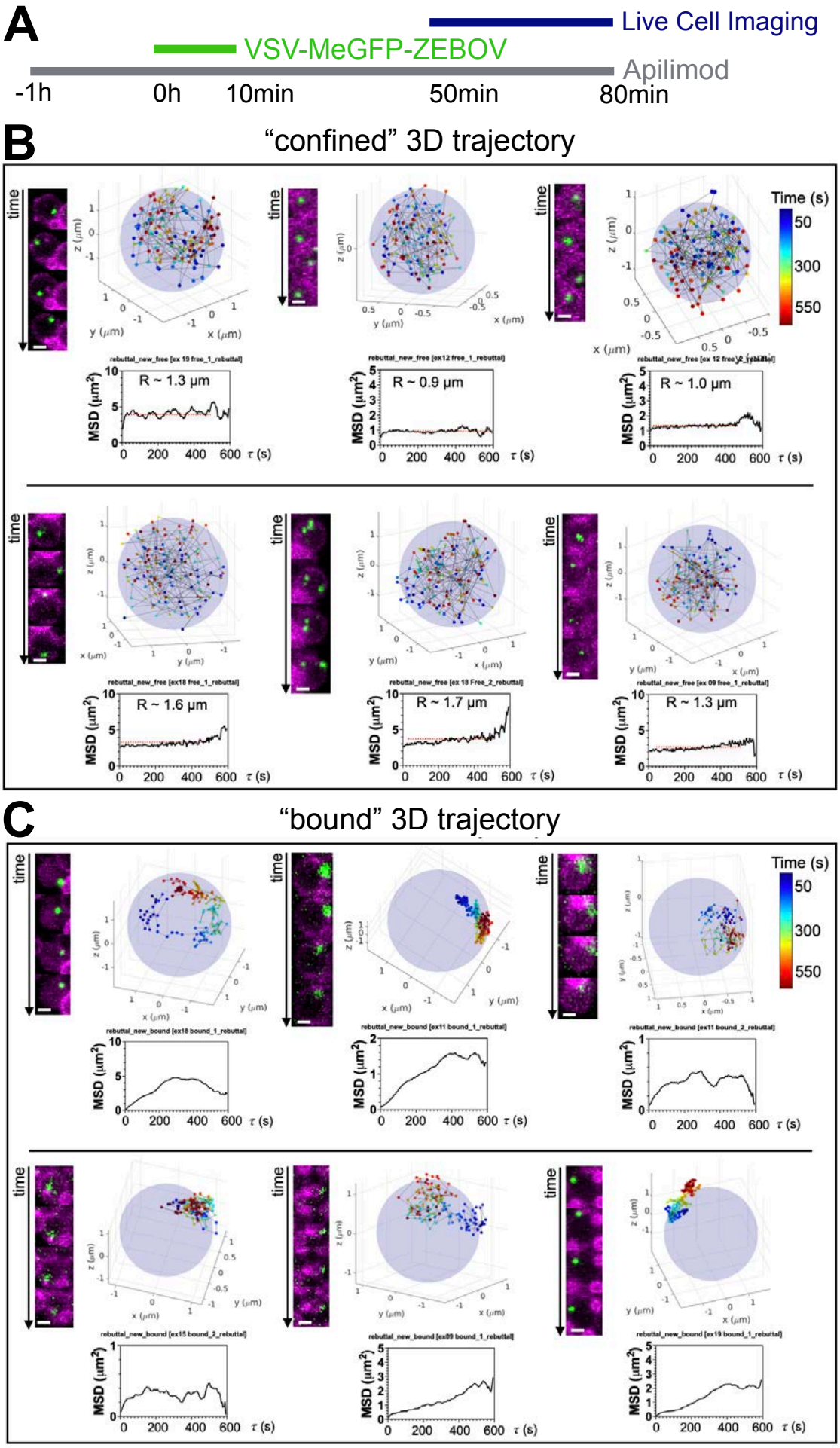
A
Live Cell Imaging
VSV-MeGFP-ZEBOV
Apilimod
-1h
0h
10min
50min
80min
B
"confined" 3D trajectory
time
Time (s)
50
300
550
R ~ 1.3 µm
R ~ 0.9 µm
R ~ 1.0 µm
R ~ 1.6 µm
R ~ 1.7 µm
R ~ 1.3 µm
MSD (µm²)
τ (s)
C
"bound" 3D trajectory

Figure S2

1184 **SI References**

1185 1. R. Zang, *et al.*, TMPRSS2 and TMPRSS4 promote SARS-CoV-2 infection of human small
1186 intestinal enterocytes. *Sci. Immunol.* **5**, eabc3582 (2020).
1187 2. Y.-L. Kang, *et al.*, Inhibition of PIKfyve kinase prevents infection by Zaire ebolavirus and
1188 SARS-CoV-2. *Proc National Acad Sci* **117**, 20803–20813 (2020).
1189 3. S. P. Whelan, L. A. Ball, J. N. Barr, G. T. Wertz, Efficient recovery of infectious vesicular
1190 stomatitis virus entirely from cDNA clones. *Proc. Natl. Acad. Sci.* **92**, 8388–8392 (1995).
1191 4. Z. Si, K. Zhou, J. Tsao, M. Luo, Z. H. Zhou, Locations and in situ structure of the polymerase
1192 complex inside the virion of vesicular stomatitis virus. *Proc. Natl. Acad. Sci.* **119**, e2111948119
1193 (2022).
1194 5. J. B. Case, *et al.*, Neutralizing Antibody and Soluble ACE2 Inhibition of a Replication-
1195 Competent VSV-SARS-CoV-2 and a Clinical Isolate of SARS-CoV-2. *Cell host & microbe* **28**,
1196 475-485.e5 (2020).
1197 6. A. C. Wong, R. G. Sandesara, N. Mulherkar, S. P. Whelan, K. Chandran, A forward genetic
1198 strategy reveals destabilizing mutations in the Ebolavirus glycoprotein that alter its protease
1199 dependence during cell entry. *Journal of virology* **84**, 163–175 (2010).
1200 7. K. Zhou, *et al.*, Atomic model of vesicular stomatitis virus and mechanism of assembly. *Nat.*
1201 *Commun.* **13**, 5980 (2022).
1202 8. M. Arzt, *et al.*, LABKIT: Labeling and Segmentation Toolkit for Big Image Data. *Front.*
1203 *Comput. Sci.* **4** (2022).
1204 9. F. Aguet, *et al.*, Membrane dynamics of dividing cells imaged by lattice light-sheet
1205 microscopy. *Molecular biology of the cell* (2016). https://doi.org/10.1091/mbc.e16-03-0164.
1206 10. L. S. V. Thomas, J. Gehrig, Multi-template matching: a versatile tool for object-localization in
1207 microscopy images. *BMC Bioinform.* **21**, 44 (2020).
1208